Pharmaceutical Sciences and Drug Design
ISSN: 3062-4428
2023, Volume 3, Page No: 270-294

Available online at: www.galaxypub.co/page/journals

Galaxy Publication

Galaxy Publication

Exploring Prenylated Xanthones as Potential Inhibitors of Ketohexokinase C Isoform for Treating Fructose-Induced Metabolic Disorders: A Comprehensive Computational Study

Rafael Silva[1], Ana P. Costa[2]*, Miguel Teixeira[1]

[1]Department of Drug Development, Faculty of Pharmacy, University of Porto, Porto, Portugal.
[2]Department of Pharmaceutical Sciences, Faculty of Pharmacy, University of Lisbon, Lisbon, Portugal.

***E-mail** ✉ ana.costa@gmail.com

Received: 24 February 2023; **Revised:** 11 May 2023; **Accepted:** 12 May 2023

ABSTRACT

Metabolic conditions linked to excessive fructose intake, including obesity, non-alcoholic fatty liver disease (NAFLD), abnormal blood lipid profiles, and type 2 diabetes, represent major worldwide public health concerns. Ketohexokinase C (KHK-C), the primary enzyme responsible for fructose phosphorylation, has emerged as an attractive target for therapeutic intervention. α-Mangostin, a prenylated xanthone derived from natural sources, has shown potent inhibitory activity against KHK-C, motivating the search for structural analogs with greater potency. The objective of this investigation was to discover α-Mangostin derivatives exhibiting stronger inhibition of KHK-C for potential use in managing these metabolic diseases. A collection of 1,383 structural analogs was assembled from publicly available chemical repositories and published studies. Candidates were evaluated through a multi-step computational pipeline involving molecular docking simulations, estimation of binding free energies, prediction of pharmacokinetic profiles, molecular dynamics trajectories, and quantum mechanical calculations. The binding affinity of α-Mangostin (−37.34 kcal/mol) was used as the reference standard. Sixteen compounds displayed binding affinities exceeding those of α-Mangostin (ranging from −45.51 to −61.3 kcal/mol), the synthetic inhibitor LY-3522348 (−45.36 kcal/mol), and previously described inhibitors obtained from marine organisms (−22.74 to −51.83 kcal/mol). Five lead compounds (designated as hits 7, 8, 9, 13, and 15) not only achieved higher binding affinities but also demonstrated more favorable drug-like and pharmacokinetic characteristics than α-Mangostin, LY-3522348, and the marine-derived compounds, suggesting improved prospects for in vivo efficacy. Of these, hit 8 stood out with the strongest binding free energy (−61.30 kcal/mol), complete predicted oral bioavailability, greater resistance to metabolic degradation, and consistent stability throughout molecular dynamics simulations. Hit 8 was identified as the top candidate owing to its exceptional binding strength, advantageous pharmacokinetic behavior, and reliable target engagement with KHK-C. These results underscore its therapeutic promise for fructose-associated metabolic syndromes and support the need for subsequent preclinical and clinical studies.

Keywords: Xanthones, Fructose, Ketohexokinase C, Obesity, Diabetes, Dyslipidemia

How to Cite This Article: Silva R, Costa AP, Teixeira M. Exploring Prenylated Xanthones as Potential Inhibitors of Ketohexokinase C Isoform for Treating Fructose-Induced Metabolic Disorders: A Comprehensive Computational Study. Pharm Sci Drug Des. 2023;3:270-94. https://doi.org/10.51847/nuISbgkTvR

Introduction

The overconsumption of fructose-rich diets has been linked to a variety of metabolic disorders, such as obesity, type 2 diabetes, non-alcoholic fatty liver disease (NAFLD), and non-alcoholic steatohepatitis (NASH), primarily by promoting insulin resistance and initiating de novo lipogenesis [1-4]. These conditions significantly reduce life expectancy and degrade quality of life on a global scale [5, 6]. Both the World Health Organization (WHO) and the American Heart Association (AHA) recommend limiting daily sugar intake to less than 5%. However, enacting this guideline worldwide is challenging due to cultural dietary patterns, widespread access to sugary foods, and varying degrees of public health awareness [6-8]. Studies suggest that excessive fructose intake is more

closely associated with negative metabolic changes than excessive glucose consumption [9-11]. Furthermore, reducing fructose intake in children has shown positive outcomes, including enhanced insulin sensitivity, reduced liver fat, and lower cardiovascular risk factors [6, 12-14], supporting the role of excessive fructose intake in metabolic disorders. Upon ingestion, fructose is rapidly processed in the liver, where the enzyme ketohexokinase (KHK) converts it to fructose-1-phosphate, using adenosine triphosphate (ATP) as a cofactor **(Figure 1)** [15, 16]. Unlike glucose metabolism, which is tightly controlled in the liver, fructose is metabolized quickly by KHK, without feedback regulation [17]. KHK exists in two isoforms—KHK-A and KHK-C—with KHK-C being the dominant form in liver fructose metabolism due to its lower KM and higher Vmax [18]. Studies on KHK-null mice have demonstrated that the absence of this enzyme protects against metabolic disorders induced by fructose, such as insulin resistance, hyperlipidemia, and weight gain [15, 19]. This evidence, alongside genetic and nonclinical studies in humans, suggests that inhibiting KHK could be a promising therapeutic strategy for managing fructose-induced metabolic disorders [20]. A review of the literature has identified three classes of small-molecule inhibitors **(Figure 2)**, with compound 1 being the most potent KHK inhibitor to date. However, rat studies have shown limited exposure to compound 1 due to high metabolic clearance [21]. Pfizer's compound 2 (PF-06835919), developed from optimizing lead compound 3, emerged as a promising candidate in phase II clinical trials for treating NAFLD [21]. In clinical trials, PF-06835919 was shown to reduce liver fat, improve insulin sensitivity, and elicit a pharmacodynamic response in human patients [6]. LY-3522348 (compound 4), developed by Eli Lilly in 2020, is another promising candidate, displaying strong inhibitory potency [22, 23]. More recently, Heine et al. reported compound 5 (BI-9787), a zwitterionic KHK inhibitor with high permeability and an ideal oral pharmacokinetic profile in rats [24]. Additionally, Alturki employed an in silico method to identify KHK-C inhibitors from natural marine organisms [5]. Other studies have shown that natural extracts and individual compounds possess potent KHK-C inhibitory effects [25]. The development of novel KHK inhibitors with better therapeutic characteristics is a critical area of research, as such inhibitors could help regulate carbohydrate metabolism while minimizing risks related to their mechanism of action [21, 26]. Nature-derived compounds and their analogs have long been a valuable source of therapeutic agents for a variety of diseases [27, 28]. Prenylated xanthones, secondary metabolites from higher plants, have demonstrated a range of biological activities, such as antioxidant [29], hepatoprotective [30], anti-inflammatory [31], anticancer [32], antimalarial [33], and antibacterial properties [34, 35]. α- and γ-Mangostins **(Figure 2),** the major prenylated xanthones found in Garcinia mangostana L. and other Garcinia species [36], have shown promising KHK-C inhibitory activity [25].

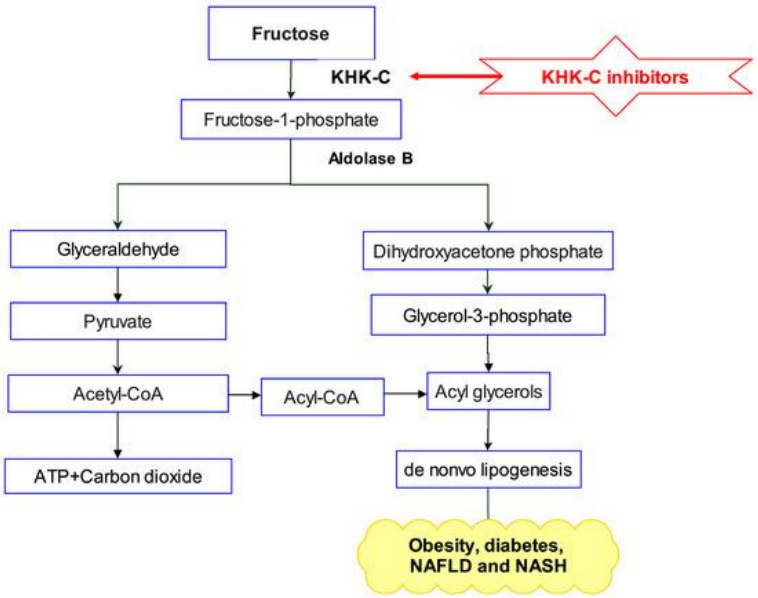

Figure 1. Fructose metabolism in the liver starts with the enzyme KHK-C catalyzing the phosphorylation of fructose, forming fructose-1-phosphate. Aldolase B then cleaves this intermediate into the trioses glyceraldehyde and dihydroxyacetone phosphate. Glyceraldehyde is further phosphorylated to produce glyceraldehyde-3-phosphate. At this point, the phosphorylated trioses enter the glycolytic pathway, eventually being converted into triglycerides and VLDL particles, thus promoting lipogenesis.

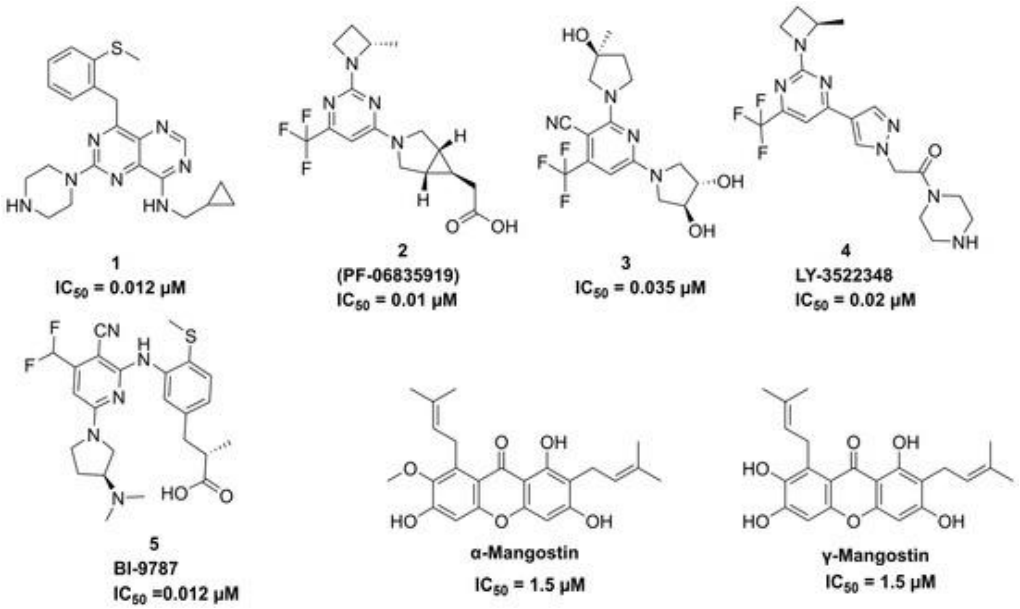

Figure 2. Structural formulas and IC50 values of known KHK-C inhibitors.

Computational methods are increasingly utilized in drug discovery for their ability to predict the therapeutic efficacy of novel compounds while conserving both time and resources [37]. In this study, we conducted a virtual screening of 1383 analogs of α- and γ-Mangostin sourced from the COCONUT database [38], PubChem [39], and relevant published research [36, 40-43]. The objective was to identify xanthones with enhanced distribution to target tissues, improved pharmacokinetics, and strong inhibitory activity against the KHK-C enzyme, a key player in fructose metabolism. The goal is that these xanthones will contribute to improved treatment strategies for metabolic disorders resulting from excessive fructose metabolism.

Materials and Methods

In this investigation, a range of computational tools from the Schrödinger suite (Schrödinger, LLC, Version: Schrödinger Software Suite 2023-1, New York, NY 10036, USA) were employed, including Protein Preparation Wizard [44], LigPrep [45], Glide [46, 47], Prime [48, 49], Qikprop [50], Jaguar [51], and Desmond [52], all accessed through the Maestro graphical interface [53].

Target selection and validation

A thorough literature review was conducted to identify high-resolution crystallographic structures suitable for docking studies from the Protein Data Bank (https://www.rcsb.org/) accessed on 20 November 2024. Among the candidates, 8UG1 (1.99 Å), 8OMJ (1.98 Å), and 9FHD (1.85 Å) were shortlisted based on their superior resolution; however, 9FHD was unavailable for download at the time of analysis. Therefore, only 8UG1 and 8OMJ were retained for comparative evaluations. To ensure the reliability of these structures, multiple structural quality assessments were conducted, including analysis of R-values, binding site density, and steric clash evaluations, with R-Free and R-Work values serving as indicators of crystallographic accuracy and model quality.

Molecular docking

A virtual screening campaign was performed on 1383 prenylated xanthones collected from the COlleCtion of Open NatUral producTs (COCONUT) Database (https://coconut.naturalproducts.net/) accessed on 25 November 2024, the PubChem Database (https://pubchem.ncbi.nlm.nih.gov/) accessed on 25 November 2024, and relevant published literature [36, 40-43]. The compound library was assembled using a Fingerprint Tanimoto-based 2D similarity search with a 95% similarity cutoff, using α-Mangostin as the query. All compounds were converted to three-dimensional representations and optimized using the OPLS4 force field. LigPrep (Schrödinger Release 2023-1) was employed to preserve the original chirality of the ligands and prepare them for docking, while Epik generated ionization states at pH 7.00 ± 2 units, with a single low-energy conformer produced per ligand.

The three-dimensional crystal structure of human KHK-C bound to the reference ligand (PDB ID: 8UG1) was retrieved from the Protein Data Bank (www.rcsb.org) accessed on 25 November 2024. The Protein Preparation Wizard (PrepWizard, Schrödinger Release 2023-1) was used to refine the protein, removing water molecules beyond 5 Å. The co-crystallized ligand in chain A was retained at the catalytic site, while the ligand in chain B was removed. Structural optimization and energy minimization were performed using the OPLS4 force field. A receptor grid centered on the reference ligand's coordinates in chain A was generated with the receptor grid generation tool in Maestro.

The prepared ligands were then docked into the optimized protein using a hierarchical docking protocol in the Glide module (Schrödinger Release 2023-1). Initial screening was carried out with high-throughput virtual screening (HTVS) to rapidly filter compounds, followed by standard precision (SP) docking for refined evaluation, and culminating in extra precision (XP) docking to achieve the most accurate predictions. Each ligand's best-scoring pose was recorded, and rankings were assigned according to Glide docking scores. For comparative purposes, LY-3522348, γ-Mangostin, and α-Mangostin were also docked, and the co-crystallized ligand underwent multiple re-docking iterations, with RMSD values calculated to validate the docking methodology.

Estimation of binding free energies

To determine the binding free energies between the protein targets and the posed compounds, the Prime tool from Schrödinger (Release 2023-1) was employed within the Schrödinger suite. The input structures were derived from the pose viewer files (PVFs) obtained post-docking, allowing calculation of binding free energies for individual molecules. The calculations incorporated the VSGB 2.0 solvent model along with the OPLS4 force field to generate relevant free energy parameters. Standard Prime parameters were maintained throughout. Ligands were subsequently ordered according to their MM–GBSA ΔG bind values, reflecting predicted binding strengths. These MM–GBSA computations were applied to the native co-crystallized compound, the advanced clinical compound LY-3522348, γ-Mangostin, and α-Mangostin to assess their respective binding energies. Further examination of the contributing energy components for the leading candidates provided deeper understanding of intermolecular forces and highlighted critical elements driving the association process.

Evaluation of ADMET characteristics

QikProp module (Schrödinger Release 2023-1) was utilized here to examine the ADMET properties and drug-like features of the leading candidates showing superior binding free energy values, in comparison with the reference clinical compound LY-3522348 and the baseline natural compound γ-Mangostin. Prior to analysis, ligand geometries were refined via LigPrep to generate optimized 3D structures and appropriate ionization states corresponding to pH 7.4. All predictions followed QikProp's standard protocols, covering essential metrics like octanol-water partition coefficient, aqueous solubility (LogS), blood-brain barrier penetration, predicted human oral bioavailability, and possible toxicity concerns. Computations were executed in standalone mode using the Schrödinger platform (Release 2023-1). The tool references established acceptable ranges for numerous descriptors, derived from 95% of approved pharmaceuticals. Output data, encompassing key descriptors and ADME forecasts, were saved to a Microsoft Excel spreadsheet.

Simulations of molecular dynamics

The Desmond package was applied to perform molecular dynamics (MD) studies on selected protein-ligand systems, encompassing the native co-crystallized compound, the clinical compound LY-3522348, γ-Mangostin, and the superior docking candidates (specifically hits 7, 8, 9, 13, and 15). These selected compounds exhibited stronger binding affinities relative to LY-3522348, coupled with promising absorption profiles and metabolic resilience. Systems were solvated using the SPC water model and positioned within an orthorhombic solvent box of 10 Å dimensions in each direction to achieve complete hydration. Sodium ions were introduced for charge neutralization, supplemented by 0.15 M NaCl to simulate physiological conditions, as described in prior work [54]. Initial energy minimization and equilibration followed Desmond's standard relaxation procedure, repeated prior to production runs. Simulations maintained 300 K temperature and 1 bar pressure under the NPT ensemble [55]. Each trajectory spanned 100 ns, capturing 1000 snapshots at 100 ps intervals. Trajectory analysis employed the Simulation Interaction Diagram tool in the Schrödinger suite (Release 2023-1), from which protein–ligand

interaction histograms, root-mean-square deviation (RMSD), root-mean-square fluctuation (RMSF), and contact mappings were derived.

Quantum chemistry computations

For the leading candidate hit 8, quantum mechanical evaluations were carried out via Density Functional Theory (DFT) in the Jaguar component of the Schrödinger package (Release 2023-1). The focus was on key electronic features, such as electron distribution and frontier orbital energies (HOMO and LUMO) [56]. These energies facilitated computation of various descriptors, including the HOMO-LUMO gap (HLG), hardness, softness, electronegativity, and electrophilicity index, using formulas from previous studies [44]. The DFT approach combined the B3LYP functional with dispersion correction (B3LYP-D3) [56]. Regions of electron deficiency appear in blue, while electron-rich areas are shown in red.

Results and Discussion

Clinical and preclinical findings have shown that KHK-C inhibition or fructose intake reduction can lead to positive outcomes in managing metabolic disorders, liver health, and kidney function [6, 57-59]. Consequently, KHK-C inhibitors are considered promising candidates for treating conditions like diabetes, obesity, NAFLD, NASH, CKD, and DKD [23, 60]. In this study, a combination of in silico approaches **(Figure 3)** was employed to screen a set of prenylated xanthones, structurally similar to α- and γ-Mangostin, as potential inhibitors of KHK-C.

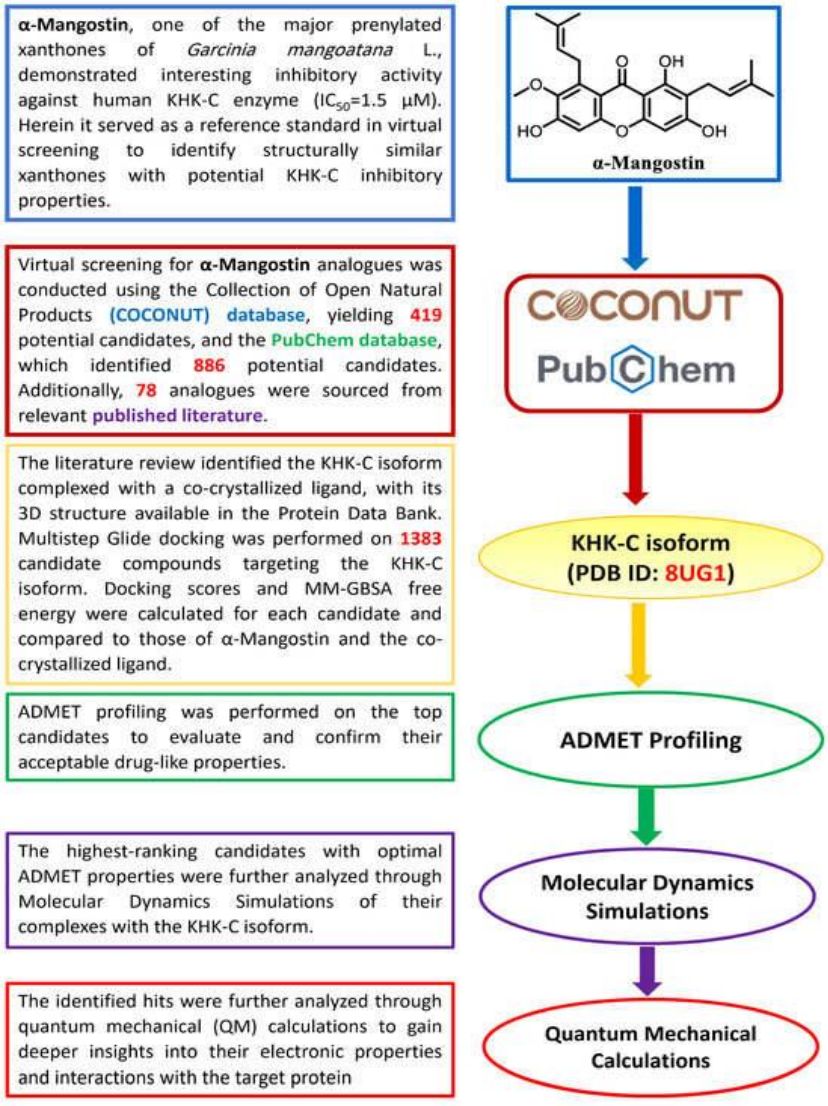

Figure 3. Pipeline for virtual screening to identify prenylated xanthones as KHK-C inhibitors.

Selection and assessment of targets

A comprehensive literature review uncovered several suitable crystal structures in the Protein Data Bank (PDB), with 8UG1 [23] (1.99 Å), 8OMJ (1.98 Å) [24], and 9FHD (1.85 Å) [24] being selected for their high resolution for docking analysis. However, 9FHD was unavailable for download, leaving only 8UG1 and 8OMJ for further evaluation. A detailed assessment of the protein structure indicated that 8UG1 was the more reliable option, based on its superior R-values (R-Free: 0.205, R-Work: 0.173) and structurally sound features, such as well-organized binding sites with minimal steric conflicts. In contrast, 8OMJ exhibited higher R-Free values (0.252) and structural issues like irregular peptide planarity and unsatisfied buried donor sites, which could affect the docking process. Consequently, 8UG1 was chosen as the most suitable candidate for the docking study.

Docking simulation

Molecular docking has become an essential approach in the field of drug discovery, helping to predict how small molecules interact with proteins at the molecular level [61, 62]. The active site of the KHK-C protein, as illustrated in **Figure 4**, is part of a dimer in the X-ray crystal structure. The co-crystallized ligand binds within the ATP site of the enzyme, primarily interacting with residues from chain A and engaging Asp27 from chain B. For this reason, docking was performed using the dimeric structure of KHK-C.

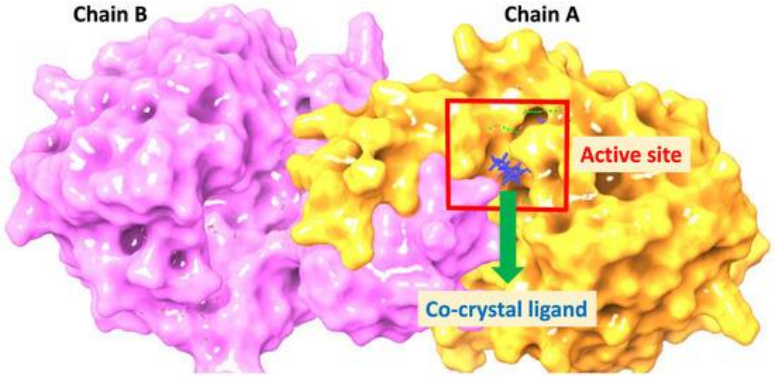

Figure 4. Mode of binding of the co-crystal ligand in the dimeric KHK-C enzyme active site.

Before initiating the virtual screening process, the co-crystal ligand underwent redocking three times to ensure the docking method's reliability **(Figure 5).** The RMSD values between the docked and original ligand poses were found to be below 0.5 Å, confirming the precision of the docking procedure. The co-crystal ligand successfully retained crucial interactions with the key residues in the active site, as shown in **Table 1 and Figure 5**. It displayed a docking score of −9.371 kcal/mol, highlighting its strong binding capacity. The ligand engaged in salt bridge interactions with Asp27 (4.1 Å) from subunit B and Glu227 (2.21 Å), in addition to several water-mediated hydrogen bonds with Ala226 (2.15 and 2.19 Å), Phe245 (2.05 and 1.91 Å), and Cys282 (2.05 and 1.78 Å), alongside a direct hydrogen bond with Glu227 (3.1 Å). The trifluoromethyl group attached to C-6 of the pyrimidine ring was involved in hydrophobic interactions with the proline loop (Pro245-Pro247), reinforcing the binding affinity. These interaction patterns were consistent with previously reported inhibitors, further validating the docking approach and the co-crystal ligand's role as a reference for screening potential KHK-C inhibitors [20, 21, 24].

The 2-hydroxymethylazetidinyl ring system, attached to the pyrimidine ring at C2, occupied the ATP-ribose pocket and formed hydrophobic interactions with residues such as Ala224, Trp225, Ala226, and Phe260. Additionally, the hydroxyl group of this ring formed a water bridge with a conserved water molecule interacting with Ala226, further enhancing binding strength. To benchmark the virtual screening hits, docking studies were also performed with γ-Mangostin, α-Mangostin [25], and LY-3522348 [23]. These compounds were compared in terms of docking scores and binding interactions with the co-crystal ligand. Given that the virtual screening hits were structural analogs of the mangostins, this comparison was particularly useful. γ-Mangostin and α-Mangostin exhibited docking scores of −7.644 and −5.992 kcal/mol, respectively, whereas LY-3522348 and the co-crystal ligand showed stronger binding with scores of −8.409 kcal/mol and −9.371 kcal/mol, respectively **(Table 1).** LY-3522348 formed similar hydrogen bond interactions with Glu227 (1.91 Å) and an additional bond with Thr253 (2.16 Å), alongside water-mediated interactions with Cys282 and Phe245, but it did not interact with Ala226,

unlike the co-crystal ligand. LY-3522348 also formed a salt bridge with Glu227 but did not interact with Asp27 **(Table 1)**.

In contrast, γ-Mangostin formed hydrogen bonds with Ala226 (1.80 Å) and displayed water-mediated interactions with Asp27, Phe245, and Cys282. These water bridges, particularly with Cys282 and Phe245, are crucial for the binding affinity of many KHK-C inhibitors [20, 21-24]. α-Mangostin showed weaker binding, forming a hydrogen bond with Glu173 and exhibiting water interactions with Lys193 and Ala226 **(Table 1)**. The importance of Lys193 and Ala226 in binding affinity has been highlighted in previous studies on potent inhibitors [23]. While γ-Mangostin shared some similarities with the co-crystal ligand in terms of key interactions, its lower docking score and lack of critical interactions like Thr253 and the salt bridges made it less favorable compared to LY-3522348. α-Mangostin, on the other hand, showed significant deviation from the co-crystal ligand's binding mode, suggesting weaker binding and lower efficacy.

Among all the compounds tested, LY-3522348 emerged as the most promising, exhibiting binding interactions most similar to those of the co-crystal ligand, and demonstrating the strongest overall binding affinity **(Table 1)**. Like the co-crystal ligand and the known inhibitor PF-06835919 [21], LY-3522348 interacted hydrophobically with the proline loop (Pro245-Pro247) through its trifluoromethyl group. In contrast, the mangostins interacted through the prenyl group at position 8. While PF-06835919 formed ionic interactions with Arg108, which are thought to be critical for its potency, LY-3522348, the co-crystal ligand, and the mangostins did not interact with Arg108. However, all compounds demonstrated similar water-mediated interactions with Cys282 and Phe245. PF-06835919 also formed hydrogen bonds with Gly255 and Gly257, interactions not seen with LY-3522348, the co-crystal ligand, or the mangostins, underscoring the importance of these residues in inhibitor binding potency [21, 24].

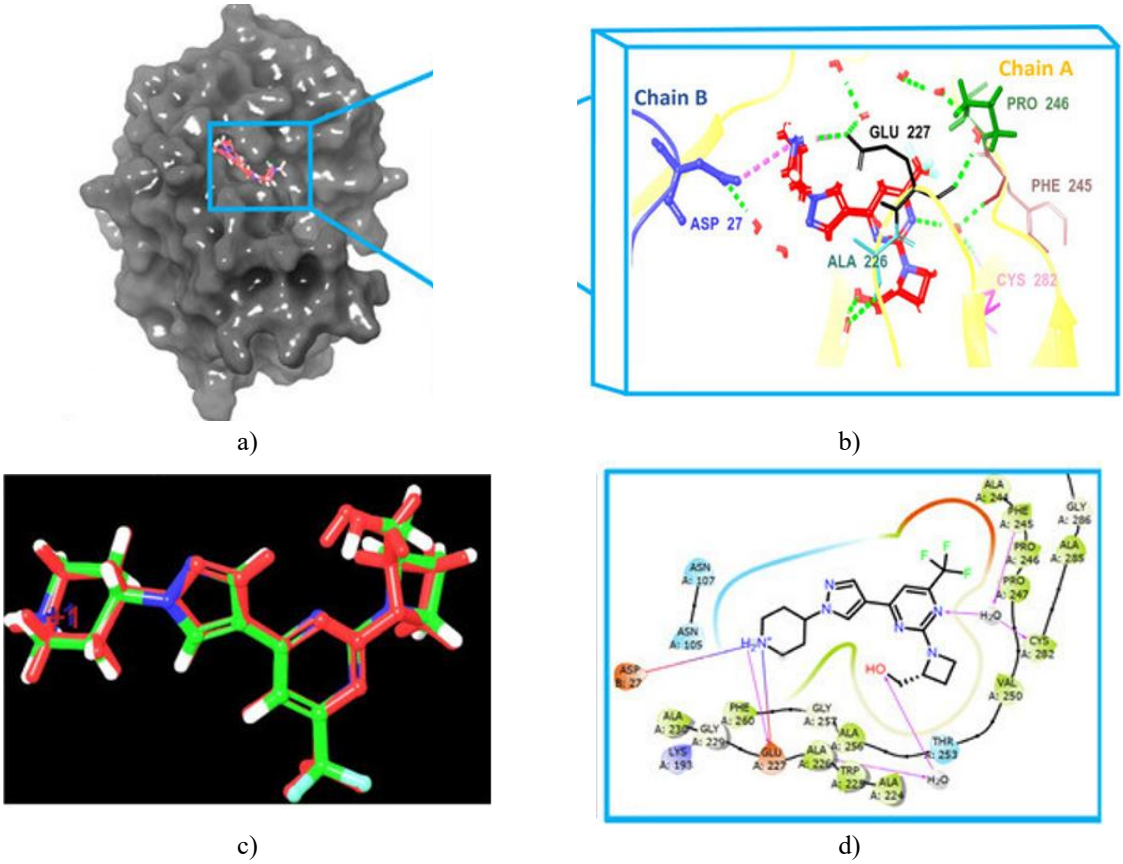

Figure 5. (a) The position of the co-crystal ligand within the KHK-C enzyme's active site (PDB ID: 8UG1).(b) 3D depiction of the interactions between the co-crystal ligand and essential active site residues, labeled with their respective three-letter codes. Green dashed lines represent hydrogen bonds and water-mediated interactions, while salt bridges are shown with pink dashed lines. (c) Illustration of the redocking procedure, where the original ligand pose is shown in green, and the redocked ligand is represented in red.(d) A two-dimensional diagram illustrating interactions, where hydrogen bonds are highlighted in magenta and

salt bridges are represented by a gradient line from purple (positive) to red (negative), indicating their electrostatic nature.

Table 1. Docking scores, molecular interactions, and bond lengths for the top 16 hits, co-crystallized ligand, clinical candidate LY-3522348, γ-Mangostin, and α-Mangostin.

NO	PubChem ID	Docking Score (kcal/mol)	Binding Energy (kcal/mol)	Interactions	
				H-Bond	Water Bridge
Co-crystal ligand		−9.371	−63.37	Glu227 (2.21 Å)	Ala226 (2.15 and 2.19 Å) Phe245 (2.05 and 1.91 Å) Cys282 (2.05 and 1.78 Å)
LY-3522348		−8.409	−45.36	Glu227 (1.91 Å) Thr253 (2.16 Å)	Phe245 (1.88 and 1.91 Å) Cys282 (1.88 and 1.78 Å)
γ-Mangostin		−7.644	−38.58	Ala226 (1.80 Å)	Asp27(1.63 and 2.01 Å) Phe245 (2.57 and 1.91 Å) Cys282 (2.57 and 1.78 Å)
α-Mangostin		−5.992	−37.34	Glu173 (1.95 Å)	Lys193 (2.17 and 2.43 Å) Ala226 (2.06 and 2.19 Å)
1	163184041	−10.791	−49.45	Ala226 (1.89 Å)	Asp27 (2.05 and 2.02 Å) Asp27 (1.57 and 2.02 Å) Phe245 (2.28 and 1.91 Å) Cys282 (2.28 and 1.78 Å)
2	–	−10.447	−40.44	Asn107 (2.31 Å) Glu227 (2.22 Å) Glu227 (2.15 Å) Glu29 (2.42 Å) Glu29 (2.17 Å) Asp194 (2.56 Å) Asp194 (2.69 Å)	Lys193 (1.98 and 2.43 Å)
3	129847812	−9.904	−54.11	Glu173 (2.11 Å) Arg108 (2.47 Å)	Phe245 (2.07 and 1.91 Å) Cys282 (2.07 and 1.78 Å) Asp27 (2.49 and 2.02 Å) Lys193 (2.27 and 2.43 Å)
4	11302345	−9.767	−37.36	Ala226 (1.88 Å)	Asp27 (1.75 and 2.02 Å) Ala226 (1.63 and 2.19 Å) Phe245 (2.31 and 1.91 Å) Cys282 (2.31 and 1.78 Å)
5	11530321	−9.626	−49.86	–	Asp27 (2.33 and 2.02 Å) Phe245 (1.97 and 1.91 Å) Cys282 (1.97 and 1.78 Å)
6	11772726	−9.444	−44.47	Asp27 (2.16 Å)	Lys193 (2.29 and 2.43 Å) Glu227 (1.83 and 2.01 Å) Phe245 (2.19 and 1.91 Å) Cys282 (2.19 and 1.78 Å)
7	129844441	−9.411	−55.13	Glu173 (1.94 Å)	Asp27 (2.32 and 2.02 Å) Lys193 (2.14 and 2.43 Å) Ala226 (1.96 and 2.19 Å) Phe245 (1.99 and 1.91 Å) Cys282 (1.99 and 1.78 Å)
8	5495931	−9.380	−61.30	Asp194 (2.48 Å)	Lys193 (1.77 and 2.43 Å) Phe245 (2.22 and 1.91 Å) Cys282 (2.22 and 1.78 Å)
9	5464633	−8.999	−53.01	–	Ala226 (1.83 and 2.19 Å) Phe245 (1.73 and 1.91 Å) Cys282 (1.73 and 1.78 Å)
10	15293189	−8.992	−45.08	Glu173 (2.19 Å) Gly255 (2.26 Å)	Ala226 (2.78 and 2.19 Å)
11	5281633	−8.991	−45.02	–	Asp27 (2.31 and 2.02 Å)

					Ala226 (2.28 and 2.19 Å) Ala226 (2.08 and 2.19 Å) Phe245 (1.95 and 1.91 Å) Cys282 (1.95 and 1.78 Å)
12	10092134	−8.978	−43.11	–	Asp27 (1.72 and 2.02 Å) Ala226 (2.32 and 2.19 Å)
13	10001484	−8.233	−59.13	–	Lys193 (2.65 and 2.43 Å) Phe245 (2.12 and 1.91 Å) Cys282 (2.12 and 1.78 Å)
14	10245099	−8.231	−44.84	Asp27 (2.09 Å)	Asp27 (1.92 and 2.02 Å) Phe245 (1.77 and 1.91 Å) Cys282 (1.77 and 1.78 Å)
15	162856452	−8.093	−45.51	Thr253 (2.76 Å)	Ala226 (1.85 and 2.19 Å) Phe245 (1.94 and 1.91 Å) Cys282 (1.94 and 1.78 Å)
16	132988553	−8.012	−42.75	–	Asp27 (1.80 and 2.02 Å) Ala226 (2.05 and 2.19 Å) Ala226 (2.33 and 2.19 Å)

A comprehensive, multi-stage molecular docking workflow was carried out on a library of 1383 prenylated xanthones, ultimately identifying 50 molecules with docking scores superior to those of γ-Mangostin and α-Mangostin. Among these, eight compounds achieved docking scores exceeding that of the co-crystallized ligand (ranging from −9.380 to −10.791 kcal/mol), and twelve outperformed the clinical candidate LY-3522348, underscoring their promise for further study. To sharpen the selection, MM–GBSA binding free-energy calculations—recognized for offering more reliable affinity estimates than docking alone [63]—were applied to these 50 candidates. This refinement yielded 16 prenylated xanthones **(Table 1 and Figure 6)** with MM–GBSA energies more favorable than those of γ-Mangostin and α-Mangostin (−38.58 and −37.34 kcal/mol, respectively). Notably, the binding energies of these compounds closely paralleled their experimental IC50 values [25], reinforcing the utility of binding affinity as a criterion for prioritizing hit compounds.

Several of the top-ranked hits—specifically compounds 1, 3, 5, 7–9, 13, and 15—displayed binding energies between −45.51 and −61.3 kcal/mol, all surpassing LY-3522348 (−45.36 kcal/mol). Hit 8 (−61.3 kcal/mol) and hit 13 (−59.13 kcal/mol) were particularly noteworthy, with hit 8 approaching the affinity of the co-crystal ligand (−63.37 kcal/mol). Both belong to the tetracyclic prenylated xanthone subclass and share a structural motif in which a prenyl substituent cyclizes with the 3-OH group to form a six-membered ring. This shared architecture likely contributes to their comparable binding strengths and highlights them as compelling candidates for further optimization and experimental validation.

The target protein's binding pocket is characterized by a relatively planar topology [24], making it especially compatible with inhibitors possessing flat, rigid scaffolds such as xanthones. The inherently planar nature of xanthones [64] enables them to align efficiently within this flat binding environment, strengthening their interactions with key residues. For instance, hit 8 **(Figure 7)** formed a hydrogen bond with Asp194 (2.48 Å) and multiple water-mediated contacts with Lys193 (1.77 and 2.43 Å), Phe245 (2.22 and 1.91 Å), and Cys282 (2.22 and 1.78 Å). It also engaged in a π–cation interaction with Arg108 (5.92 Å). Residues including Cys282, Phe245, and Lys193 have been repeatedly identified as crucial contributors to inhibitor binding, while Arg108 is known to enhance inhibitor potency [21, 24]. Hit 13 **(Figure 7)** exhibited a similar interaction profile, forming water bridges with Lys193 (2.65 and 2.43 Å), Phe245 (2.12 and 1.91 Å), and Cys282 (2.12 and 1.78 Å). The recurrence of these residues across multiple hits underscores their importance as interaction hotspots and further validates xanthones as a structurally compatible inhibitor class.

Across all 16 prioritized hits, a broadly consistent interaction pattern was observed **(Table 1)**, though individual compounds displayed subtle differences in residue engagement. Most notably, the majority formed interactions with Phe245 and Cys282—residues widely recognized as central to ligand binding—while hits 10, 12, and 16 were exceptions, lacking interactions with both. Distinctive interactions were also noted: hits 8 and 10 each formed π–cation contacts with Arg108 (5.92 Å and 4.45 Å, respectively), and hit 4 established a salt bridge with Arg108 (3.35 Å). The polyamine-containing hit 2 stood out for its extensive electrostatic network, forming two ionic interactions with Glu29 (3.21 Å and 3.44 Å), two with Asp194 (4.71 Å and 3.26 Å), and one with Glu227 (4.34

Å). These variations highlight the diversity of binding modes among the hits and emphasize the pivotal role of these residues in shaping binding affinity and potential inhibitory activity.

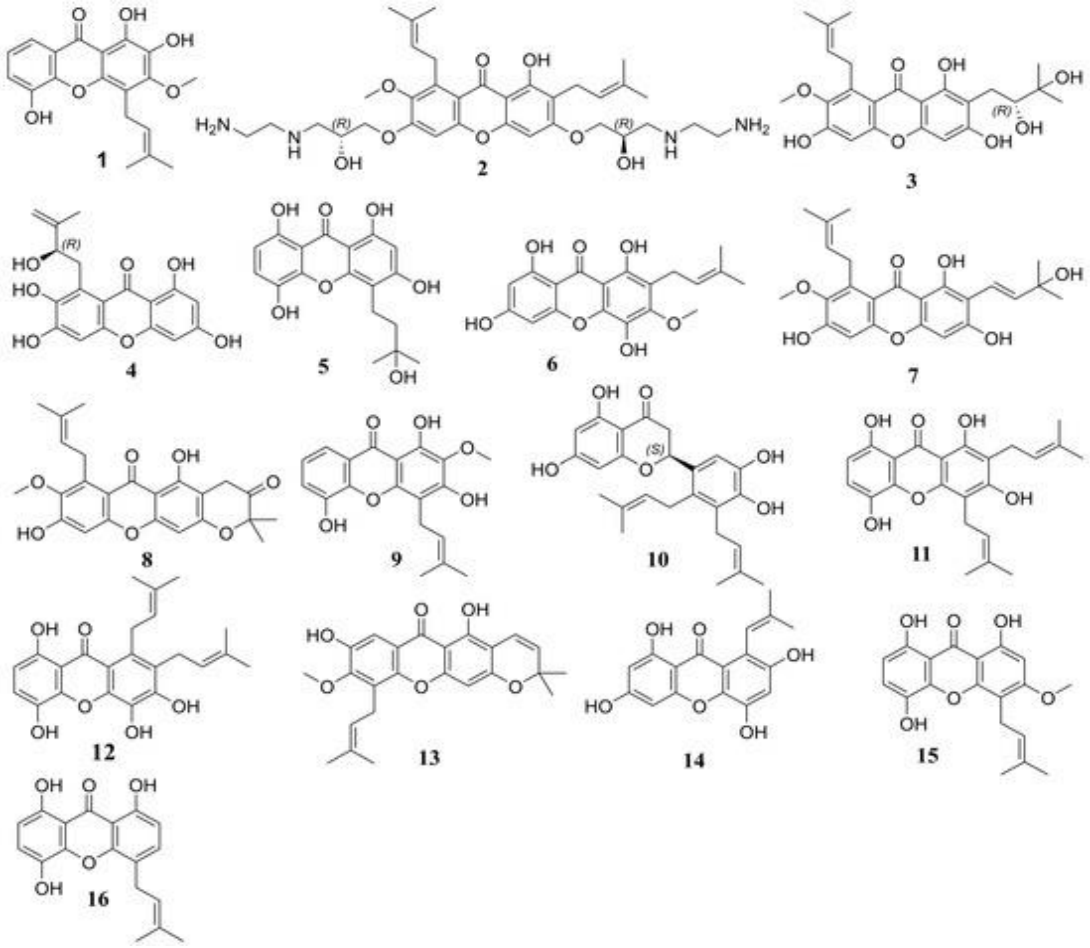

Figure 6. Structural representations of the primary hit compounds obtained from the virtual screening workflow.

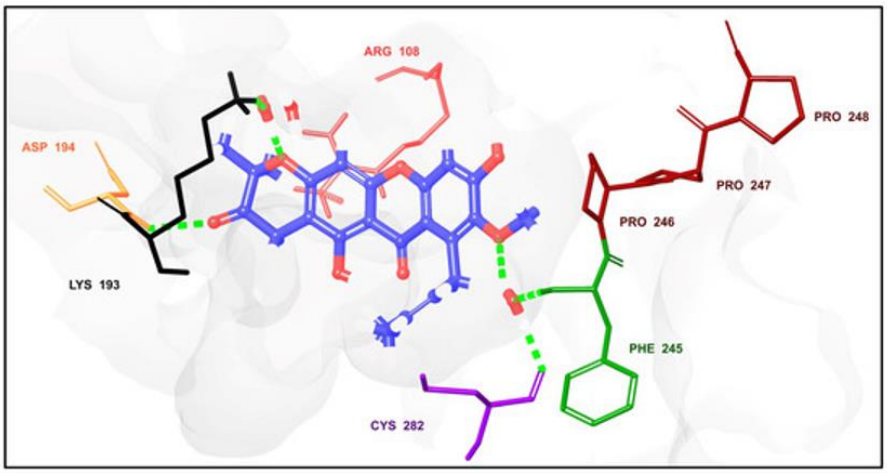

a)

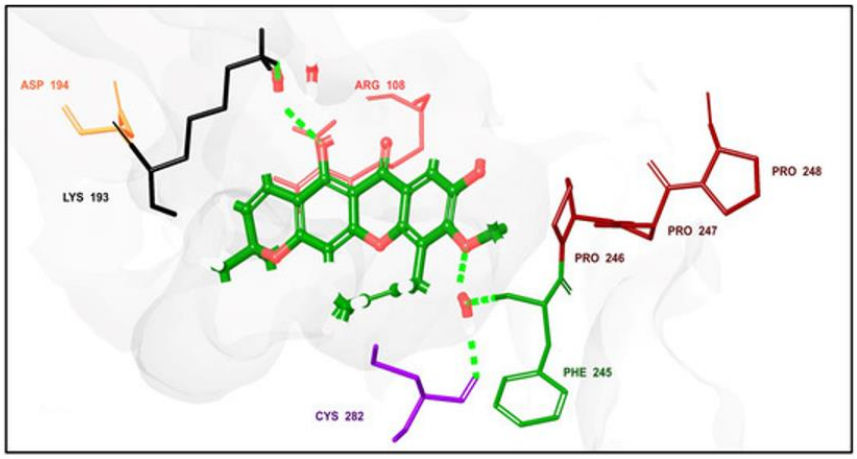

b)

Figure 7. 3D binding modes of two prenylated xanthones, designated as hit 8 (panel a) and hit 13 (panel b), within the active site of KHK-C (PDB ID: 8UG1). These visualizations emphasize critical amino acid contacts, including hydrogen bonds and water-mediated bridges (shown in green) as well as π-cation interactions (depicted in red).

A structure-activity relationship (SAR) evaluation was additionally performed on the leading compounds, hits 8 and 13, to elucidate the impact of specific structural elements on their binding strengths and to inform subsequent lead optimization efforts as prospective KHK inhibitors. To this end, six derivatives were proposed for hit 8 and another six for hit 13 **(Figure 8),** enabling a deeper investigation into potential improvements in target engagement. Every derivative derived from hit 8 (labeled I–VI) displayed reduced binding energies (spanning −19.43 to −52.6 kcal/mol) relative to the parent hit 8, suggesting that hit 8 already incorporates the optimal functional groups necessary for strong protein-ligand contacts. By comparison, certain derivatives of hit 13—namely VII and XI—showed markedly improved binding energies of −66.75 and −64.80 kcal/mol, respectively. These figures exceeded the values for both the original hit 13 (−59.13 kcal/mol) and the co-crystallized reference ligand (−63.37 kcal/mol), underscoring their greater potential for favorable binding. The key distinction in analog VII from hit 13 involves substitution of the methoxy substituent at position 9 with an extra hydroxyl group, thereby boosting polarity and facilitating additional hydrogen bonds. In analog XI, the absence of the double bond within the pyrano ring distinguishes it from hit 13; this alteration probably enhances overall rigidity and conformational stability, promoting stronger hydrophobic contacts and improved accommodation in the binding pocket. Such changes are presumed to underpin the superior binding observed in these two derivatives. Importantly, both VII and XI are readily preparable via a single synthetic step from hit 13, rendering them practical and economical candidates for advanced studies. Conversely, the remaining derivatives showed substantially weaker binding energies (from −21.65 to −53.38 kcal/mol), implying that those alterations interfered with essential contact networks and diminished inhibitory performance.

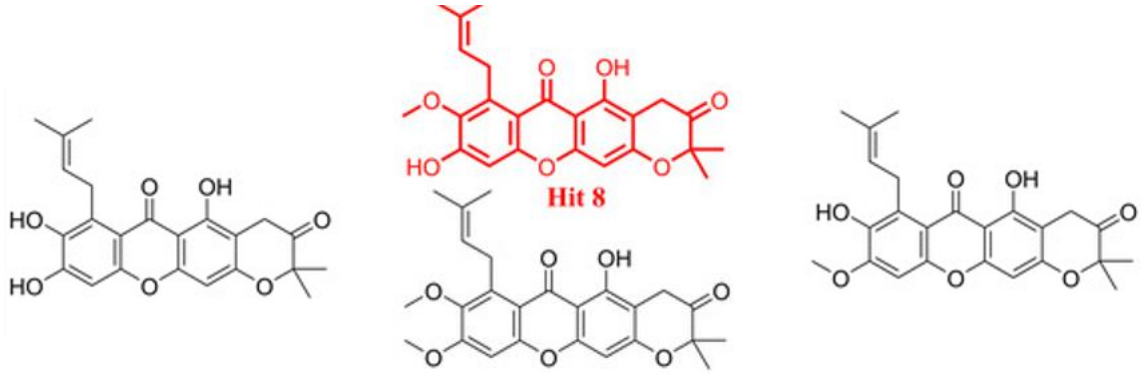

I II III

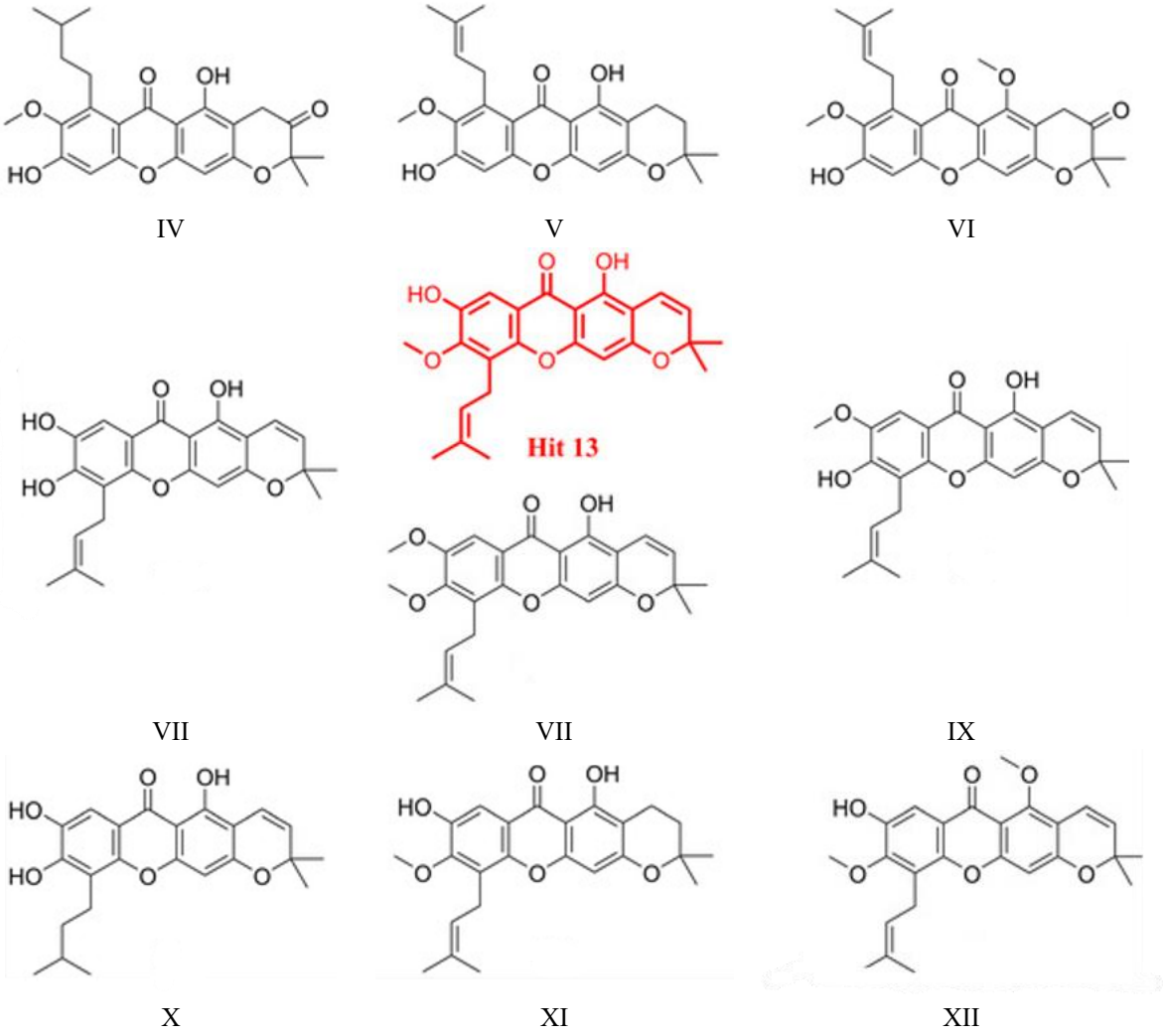

Figure 8. Structures of the proposed analogs based on hit 8 (labeled I–VI) and hit 13 (labeled VII–XII).

For additional context, a comparison was performed between the leading prenylated xanthones discovered in this work and the five most potent marine-sourced natural product inhibitors described by Alturki [5] **(Figure 9).** The evaluation centered on their respective binding affinities toward KHK-C (PDB ID: 8UG1). According to the data presented in **Tables 1 and 2**, the prenylated xanthones from the current investigation—namely hits 3, 7, 8, 9, and 13—showed superior binding affinities (ranging from −53.01 to −61.30 kcal/mol) in comparison to the marine-derived compounds (ranging from −22.74 to −51.83 kcal/mol). In particular, hits 8 (−61.30 kcal/mol) and 13 (−59.13 kcal/mol) displayed substantially stronger binding, reinforcing their advantageous binding characteristics. Overall, these results indicate that the prenylated xanthones uncovered here represent more attractive leads than the marine natural products previously reported by Alturki [5], underscoring the greater promise of the present hits for subsequent optimization and development.

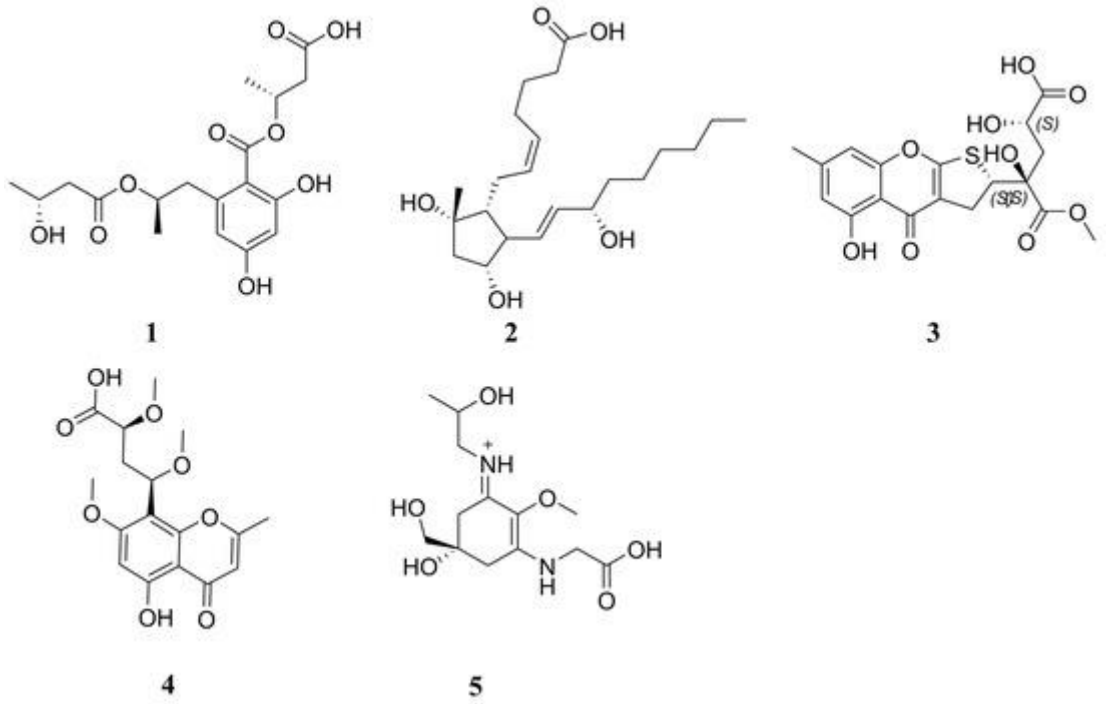

Figure 9. Chemical structures of the top five marine-derived natural product inhibitors identified by Alturki and reported as potential inhibitors of KHK-C.

Table 2. Docking scores and binding energies of the top 5 marine-derived natural products.

Compounds	Binding Free Energy (kcal/mol)	Docking Score (kcal/mol)
1	−22.74	−9.395
2	−32.06	−7.402
3	−44.39	−8.810
4	−37.87	−7.704
5	−51.83	−8.894

Binding free energy calculations and MM–GBSA decomposition analysis

This section presents a detailed examination of the binding strengths and interaction patterns for the leading compounds, hit 8 and hit 13. For benchmarking purposes, γ-Mangostin and the co-crystallized ligand LY-3522348 were included as reference standards. The primary objective was to pinpoint the critical elements driving molecular recognition and overall binding performance, thereby offering valuable guidance on the inhibitory potential of these agents.

The decomposition of binding free energies and interaction profiles for LY-3522348 (the co-crystal ligand), γ-Mangostin, hit 8, and hit 13 are depicted in **Figure 10.** Among these, the co-crystal ligand achieved the highest binding free energy of −63.37 kcal/mol, establishing it as the reference standard. Hit 8 was a close second with −61.30 kcal/mol, while hit 13 exhibited a similar value of −59.13 kcal/mol. In marked contrast, γ-Mangostin and LY-3522348 recorded substantially weaker energies of −38.58 kcal/mol and −45.36 kcal/mol, respectively.

Coulomb electrostatic contributions **(Figure 10)** were particularly pronounced for γ-Mangostin (−29.44 kcal/mol) and the co-crystal ligand (−28.87 kcal/mol), emphasizing the role of polar contacts in their binding. Conversely, LY-3522348 showed the least favorable Coulomb term (−11.12 kcal/mol), which notably constrained its overall affinity.

Van der Waals (vdW) interactions, representing key hydrophobic forces, emerged as dominant drivers of binding across all molecules **(Figure 10).** The co-crystal ligand displayed the strongest vdW contribution (−55.77 kcal/mol), closely followed by hit 13 (−54.74 kcal/mol) and hit 8 (−50.24 kcal/mol). γ-Mangostin, with a more modest vdW term (−36.49 kcal/mol), was disadvantaged in this regard.

The solvation free energy penalty (Solv GB) exerted an unfavorable effect in every case, with the largest penalties observed for γ-Mangostin (35.48 kcal/mol) and the co-crystal ligand (35.13 kcal/mol). Packing energies, indicative of geometric complementarity and binding stability, were most favorable for hit 13 (−18.85 kcal/mol)

and hit 8 (−15.95 kcal/mol). Hydrogen bonding terms provided moderate but meaningful stabilization across the set.

From a structural perspective, the trifluoromethyl group and aromatic systems of the co-crystal ligand supported robust polar and hydrophobic contacts. Although LY-3522348 possesses polar functionalities, its poor electrostatic contribution undermined its performance. The hydroxyl-rich xanthone core of γ-Mangostin promoted strong polar interactions, yet insufficient vdW forces and elevated solvation costs reduced its effectiveness. As pyranoxanthone derivatives, hit 8 and hit 13 shared comparable overall profiles: hit 8 benefited from superior vdW interactions, whereas hit 13 stood out due to enhanced packing energy, conferring greater conformational stability.

Collectively, hit 8 and hit 13 proved to be the most competitive candidates, owing to their well-balanced and favorable energy components. γ-Mangostin, despite its inferior total binding, retained merit in scenarios favoring electrostatic dominance. This analysis successfully linked the MM–GBSA decomposition results to the structural features of hits 8 and 13, elucidating their binding mechanisms and laying a solid foundation for future structural refinement and optimization.

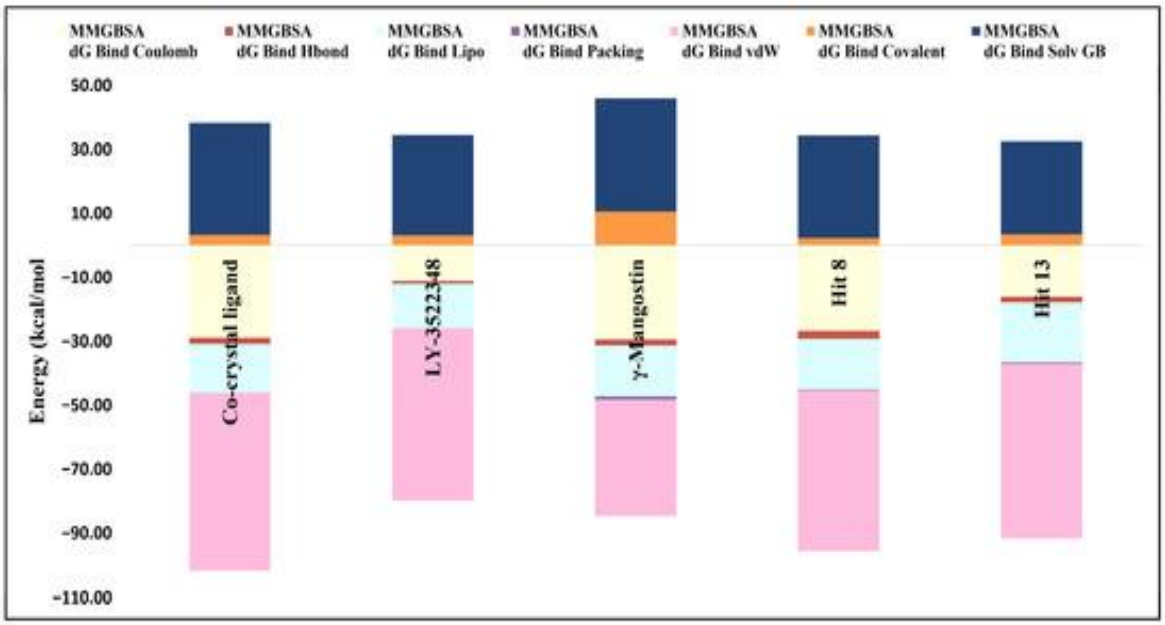

Figure 10. Breakdown of energy components for the co-crystal ligand, LY-3522348, γ-Mangostin, hit 8, and hit 13.

ADMET profiling

In silico assessment of drug-like properties during the initial stages of drug discovery is essential [65]. These predictive computational techniques enable the examination of key attributes, including molecular weight, solubility, membrane permeability, and toxicity risks. By prioritizing compounds with desirable profiles and eliminating those with unfavorable characteristics early on, such tools streamline the discovery process, enhance efficiency, and improve overall success rates [66, 67].

In this study, the ADMET characteristics of the top 16 hits were determined and benchmarked against LY-3522348 and γ-Mangostin. The objective was to gauge the alignment of these hits with ideal drug-like features and to evaluate their suitability for advancement as therapeutic leads.

A composite ADME compliance score—expressed as drug-likeness (#stars)—was employed to measure deviation from properties typical of approved drugs. This metric reflects how many descriptor values lie outside the 95% confidence interval derived from known therapeutics [68, 69]. Here, LY-3522348 and the majority of hits (1, 3–9, and 13–16) achieved a score of zero, meaning all their descriptors fell within the 95% range of established drugs, demonstrating outstanding drug-likeness. γ-Mangostin and hits 10, 11, and 12 received a score of one, indicating minor deviations yet still acceptable compliance. In contrast, hit 2 scored eight, revealing substantial departures from standard drug-like ranges and raising significant concerns about its viability as a development candidate.

Physicochemical attributes critical to therapeutic performance—such as molecular size, solubility, and lipophilicity—were also analyzed [70]. Molecular weights spanned 312.3 (hit 16) to 444.5 (hit 3), all comfortably within the acceptable 130–725 range, confirming suitable dimensions for drug candidates. Solvent-accessible surface area (SASA) values ranged from 525.5 (hit 16) to 710.4 (hit 7), falling entirely within the recommended 300–1000 limits, indicative of appropriate solvent interactions.

Compounds exhibiting poor membrane permeability often suffer from suboptimal ADME outcomes, leading to diminished efficacy [70]. Membrane crossing capability directly governs absorption and bioavailability [71]. Polar surface area (PSA), a widely used predictor of permeability [72], varied from 86.3 (hit 13) to 177.5 (hit 2) across the set, remaining within the favorable 7–200 range and suggesting efficient transit across biological barriers. Hydrogen bond donors (donorHB) ranged from 1 (hits 8, 13, 15, 16, and LY-3522348) to 4 (hits 3 and 4), well inside the 0–6 limit; however, hit 2 displayed eight, exceeding norms and likely impairing permeability and bioavailability. Hydrogen bond acceptors (accptHB) spanned 2.8 (hit 16) to 12.9 (hit 2), complying with the 2–20 threshold. These balanced polar features support favorable hydrophilic–hydrophobic interplay, vital for oral bioavailability—a key advantage of small-molecule therapeutics, particularly since oral dosing is preferred over other routes [73].

Given that oral administration is highly desirable for agents targeting fructose-related metabolic conditions (as seen in recent candidates [21, 23, 24]), and considering that some reported potent KHK-C inhibitors display only low-to-moderate bioavailability, the oral absorption potential of the hits was specifically examined. Hits 8 and 13 achieved perfect 100.0% predicted oral bioavailability, with hit 11 close behind at 95.8%, marking them as outstanding prospects for oral therapeutics with efficient absorption. Hits 7, 9, 15, and 16 also exhibited strong values (>90%). Conversely, hit 2 showed 0.0%, likely due to excessive polarity, size, or instability. Hits 4, 5, and 14 displayed moderate levels, potentially amenable to optimization via structural modifications or formulation strategies.

Relative to LY-3522348 (80.35%) and γ-Mangostin (92.30%), many hits outperformed these references in predicted bioavailability. Furthermore, compared to marine-derived natural products previously reported (17.6–59.3% oral absorption [5]), the current hits demonstrated markedly superior absorption, reinforcing their enhanced therapeutic promise through better oral delivery.

Intestinal permeability, assessed via QPPCaco values, varied considerably. LY-3522348 registered 165.9 (moderate), while γ-Mangostin reached 269.5. Hits 13 (715.6) and 8 (675.4) exceeded the high-permeability threshold (>500), with hits 16 (417.7), 9 (415.5), and 7 (303.2) still surpassing the references, supporting improved bioavailability.

Plasma protein binding influences pharmacokinetic and pharmacodynamic behavior; high binding can extend duration but reduce free drug levels [74]. QPlogKhsa predictions identified hits 11, 13, and γ-Mangostin with the strongest binding (>0.5). LY-3522348, hit 2, hit 4, and hit 14 showed weaker binding (<0), with hit 4 lowest (−0.3). The remaining hits displayed moderate binding, suggesting prolonged circulation and potential for less frequent dosing alongside sustained efficacy.

hERG channel blockade poses a major cardiotoxicity risk in drug development [75]. QPlogHERG values classified hit 2 (−9.0) as high risk (<−6). γ-Mangostin (−5.341) and hit 13 (−5.5) fell into moderate risk (−5.0 to −6.0), while most others, including LY-3522348 (−4.651) and hit 1 (−4.6), indicated low risk (>−5.0), reflecting safer cardiac profiles.

Metabolic stability, gauged by predicted metabolite count (acceptable 1–8) [76], showed the hits generally outperforming γ-Mangostin (10 metabolites). LY-3522348 had only one, denoting excellent stability. Several hits (e.g., 5, 13, 14, 16 with six; 1, 4, 8, 15 with seven; 6, 7, 9 with eight) remained within range. Hits 3, 10, 11, and 12 matched γ-Mangostin at 10, while hit 2 reached 18, signaling greater instability.

All compounds complied with Lipinski's Rule of Five (≤4 violations) and Veber's Rule of Three (≤3 violations), affirming strong oral bioavailability potential and appropriate pharmacokinetics.

In summary, this ADMET evaluation underscores the attractive drug-like profiles of multiple hits, characterized by excellent absorption, permeability, and stability. Hits 8 and 13, in particular, stand out with superior oral bioavailability and balanced properties, positioning them as highly promising leads for subsequent preclinical advancement.

Molecular dynamics (MD) simulations

Five selected hits—specifically hits 7, 8, 9, 13, and 15—were chosen for molecular dynamics simulations based on their superior binding affinities compared to the clinical candidate LY-3522348 (better than −45.36 kcal/mol), oral bioavailability greater than 90%, and acceptable metabolic stability. The primary objective was to explore the dynamic characteristics of these compounds at an atomic level and to examine the nature, strength, and persistence of their interactions with KHK-C.

For benchmarking, γ-Mangostin, LY-3522348, and the co-crystallized ligand were also subjected to parallel simulations.

Molecular dynamics simulations are a well-established computational technique in drug discovery, providing critical information on the stability, conformational flexibility, and binding interaction patterns of ligand–protein complexes under conditions mimicking physiological environments [63].

The root-mean-square deviation (RMSD) and root-mean-square fluctuation (RMSF) metrics for the simulated systems are compiled in **Table 3** and illustrated in **Figure 11** (RMSD) and **Figure 12** (RMSF), yielding key insights into their dynamical properties.

In the RMSD analysis **(Figure 11),** the ligand-free (Apo) protein displayed an average deviation of 2.9 Å, indicating moderate structural variability. The co-crystal ligand complex showed a higher average RMSD of 4.4 Å, suggesting greater conformational shifts from the starting structure. By comparison, hits 7 and 8 achieved lower averages of 2.6 Å and 2.7 Å, respectively, demonstrating enhanced structural stability relative to the other systems.

Hits 7 and 8 also exhibited markedly superior stability when contrasted with previously reported top marine-derived inhibitors [5], as reflected in their lower RMSD values and consistently flat trajectories over the simulation timeframe. These results highlight the exceptional dynamic performance and robust fitting of hits 7 and 8 within the binding pocket, positioning them as particularly strong candidates for advancement.

The co-crystal ligand displayed pronounced fluctuations between 40 and 70 ns, indicative of transient instability, while hit 15 showed large deviations throughout the full 100 ns trajectory, pointing to reduced overall stability. In contrast, hits 7 and 8 reached equilibrium rapidly and sustained stable profiles across the entire simulation, further supporting their reliable binding characteristics. Peak RMSD values reinforced this pattern, with the co-crystal ligand (6.8 Å) and hit 15 (6.3 Å) registering the largest deviations, whereas hits 7 and 8 maintained considerably lower maxima, confirming greater binding persistence.

The RMSF evaluation **(Figure 12)** provided residue-specific flexibility details that aligned with the RMSD observations. The Apo form, hit 7, and hit 8 recorded low average RMSF values of 1.6 Å, 1.6 Å, and 1.4 Å, respectively, reflecting minimal overall fluctuations. LY-3522348 exhibited the highest peak RMSF of 14.3 Å, indicating substantial mobility in certain regions.

Across all complexes, residues 300–307—situated in the terminal loops at the A–B subunit interface of KHK-C—consistently showed elevated flexibility, identifying this segment as a flexible hinge region. This intrinsic mobility likely facilitates inter-subunit signaling and modulates ligand accommodation dynamics.

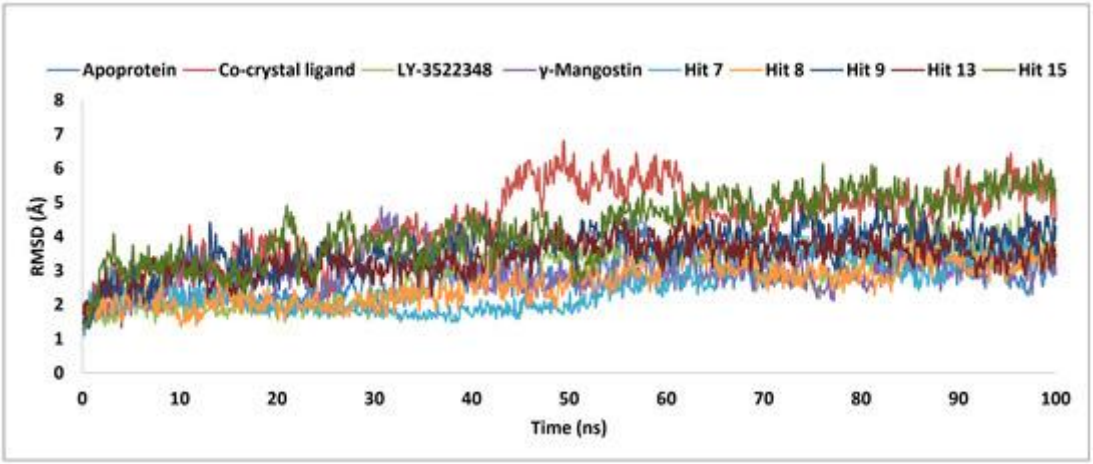

Figure 11. Root mean square deviation (RMSD) evaluation of compounds 7, 8, 9, 13, 15, γ-Mangostin, LY-3522348, the co-crystallized ligand, and the unbound protein throughout 100 ns molecular dynamics simulations.

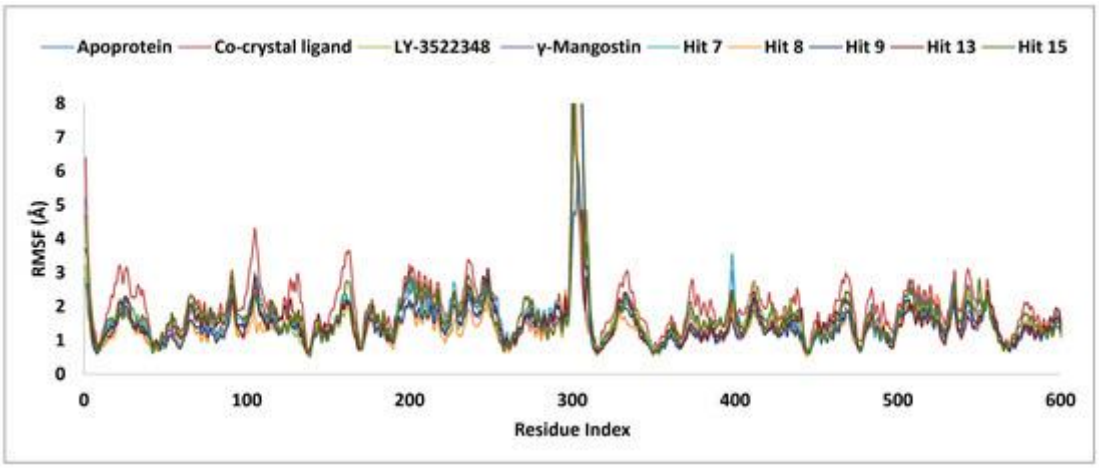

Figure 12. Root mean square fluctuation (RMSF) evaluation of compounds 7, 8, 9, 13, 15, γ-Mangostin, LY-3522348, the co-crystallized ligand, and the ligand-free protein, illustrating amino acid residue flexibility across 100 ns molecular dynamics simulations.

Table 3. Root Mean Square Deviation (RMSD), Root Mean Square Fluctuation (RMSF), and ligand–protein interaction profiles (including hydrogen bonds, water bridges, hydrophobic interactions, and π–cation interactions) for the apo protein, co-crystallized ligand, LY-3522348, γ-Mangostin, and the five top-scoring compounds throughout a 100 ns molecular dynamics simulation.

KHK-C Complex	Co-Crystal Ligand	Apo	LY-3522348	γ-Mangostin	Hit 15	Hit 13	Hit 9	Hit 8	Hit 7
Protein–Ligand RMSD (Å)									
Average	4.4	2.9	2.9	2.9	4.2	3.4	3.6	2.7	2.6
Maximum	6.8	4.8	4.6	4.8	6.3	4.9	5.1	4.9	4.2
Minimum	1.3	1.3	1.3	1.2	1.3	1.6	1.3	1.3	1.1
Protein RMSF (Å)									
Average	2.1	1.6	1.6	1.5	1.7	1.6	1.5	1.4	1.6
Maximum	13.7	5.5	14.3	9.5	7.8	8.0	12.3	11.2	8.9
Minimum	0.7	0.6	0.6	0.6	0.5	0.6	0.6	0.5	0.5
Hydrogen bond contacts									
Average	0.5	-	1.1	2.7	-	-	-	0.5	-
Maximum	3.0	-	3.0	4.0	-	-	-	3.0	-
Minimum	0.0	-	0.0	0.0	-	-	-	0.0	-
Hydrophobic contacts									
Average	0.5	-	0.8	1.2	-	-	-	2.0	-
Maximum	3.0	-	4.0	5.0	-	-	-	6.0	-
Minimum	0.0	-	0.0	0.0	-	-	-	0.0	-
Water bridge contacts									
Average	2.7	-	1.8	0.8	-	-	-	1.2	-
Maximum	7.0	-	7.0	7.0	-	-	-	6.0	-
Minimum	0.0	-	0.0	0.0	-	-	-	0.0	-

To further investigate the stability of the compounds within the binding pocket, separate root mean square fluctuation (RMSF) assessments were conducted for key active-site residues. Residues such as Gly106, Asn107, and Arg108 displayed different levels of flexibility depending on the bound ligand, as indicated by their RMSF values. The co-crystallized ligand induced the greatest flexibility in these residues, with RMSF ranging from 2.7 Å to 3.8 Å, suggesting considerable conformational dynamics in the binding region. The ligand-free protein (apoprotein) showed intermediate fluctuations, with values between 1.7 Å and 2.2 Å. γ-Mangostin produced marginally reduced flexibility relative to the apoprotein, with RMSF values from 1.9 Å to 2.3 Å. By comparison, hit 8 displayed the least flexibility of all evaluated systems, with values between 1.2 Å and 1.5 Å, underscoring

its robust and consistent engagement with these essential residues. Hit 7 exhibited somewhat greater flexibility than hit 8, ranging from 2.2 Å to 2.8 Å, whereas LY-3522348 maintained intermediate flexibility, with RMSF values from 1.7 Å to 2.3 Å. These differences emphasize the enhanced stability provided by hit 8 and, to a slightly lesser degree, hit 7, relative to γ-Mangostin, LY-3522348, and the co-crystallized ligand.

For Lys193, flexibility varied across systems, with hit 8 recording the lowest RMSF of 1.35 Å, indicative of excellent stability. In contrast, the co-crystal ligand showed the highest value at 2.1 Å, followed by the apoprotein (1.8 Å), γ-Mangostin (1.84 Å), and LY-3522348 (1.4 Å), reflecting a spectrum from moderate to low mobility. Hit 8 also achieved the greatest stability at Gly255 and Gly257, with RMSF values of 0.94 Å and 0.78 Å, respectively, surpassing all other ligands and demonstrating minimal movement at these important binding-site positions. Furthermore, Phe260, a component of the hydrophobic subpocket [21], exhibited an RMSF of 0.76 Å with hit 8, signifying limited structural variation and consistent occupancy of this non-polar region throughout the simulation. This contact with Phe260 supported the overall integrity of the hydrophobic subpocket and reinforced the binding affinity of hit 8.

At Asp27, a vital residue in subunit B [23], hit 8 again provided the highest stability, with an RMSF of 1.4 Å, outperforming the co-crystal structure (3.0 Å), γ-Mangostin (2.2 Å), and LY-3522348 (2.2 Å), further confirming its favorable engagement across the pocket. Similarly, Cys282 and Phe245—key active-site residues that participate in water-mediated bridges commonly observed with known inhibitors [5, 21, 23, 24]—displayed RMSF values of 1.1 Å and 1.8 Å, respectively, in the presence of hit 8. These figures were lower than those for the other ligands, pointing to reduced conformational changes and greater steadiness at these positions. Thr253, another crucial active-site residue, showed an RMSF of 1.2 Å with hit 8, again lower than in the other systems, indicating diminished fluctuations and improved stabilization.

Overall, the RMSF evaluation revealed that hit 8 conferred exceptional stability on critical binding-site residues, including Lys193, Gly106, Asn107, Arg108, Gly255, Gly257, Phe260, Asp27, Cys282, Phe245, and Thr253, outperforming the other compounds. The reduced mobility at these sites suggests that hit 8 substantially strengthens protein–inhibitor contacts, positioning it as a potentially potent and reliable inhibitor for the target enzyme's active site. With its favorable average RMSD of 2.7 Å and outstanding capacity to rigidify key pocket residues relative to the benchmark ligands, hit 8 was chosen for in-depth interaction profiling, detailed in **Table 3** and **Figure 13**. This examination sheds light on the mechanisms underlying its superior behavior compared to the remaining candidates, solidifying its promise as a lead molecule.

As illustrated in **Figure 13a**, hit 8 formed an average of 0.5 hydrogen bonds, comparable to the co-crystal ligand but markedly fewer than γ-Mangostin (2.7) and LY-3522348 (1.1), implying relatively limited direct polar bonding. Nevertheless, hit 8 excelled in hydrophobic contacts **(Figure 13b),** registering the highest average (2.0) and peak (6.0) among the evaluated compounds, which highlights its robust stabilization of the pocket via non-polar interactions. For water-mediated bridges **(Figure 13c)**, hit 8 achieved an average of 1.2, exceeding LY-3522348 (0.8) though trailing γ-Mangostin (1.8) and the co-crystal ligand (2.7), consistent with intermediate water-bridging contributions.

Although hit 8 showed lower averages for hydrogen bonding and water bridges, its dominant hydrophobic interactions compensated effectively, yielding a well-rounded binding mode with strong potential to secure the KHK-C active site. These extensive non-polar engagements were absent in the reference compounds, distinguishing the unique interaction pattern of hit 8. The pronounced hydrophobic profile substantially bolstered pocket stabilization, complementing the quantitative data in **Figures 13a–13c**. Despite reduced polar and water-mediated contributions, the exceptional hydrophobic interactions of hit 8 establish it as a highly effective candidate for reliable occupancy and stabilization of the KHK-C binding site.

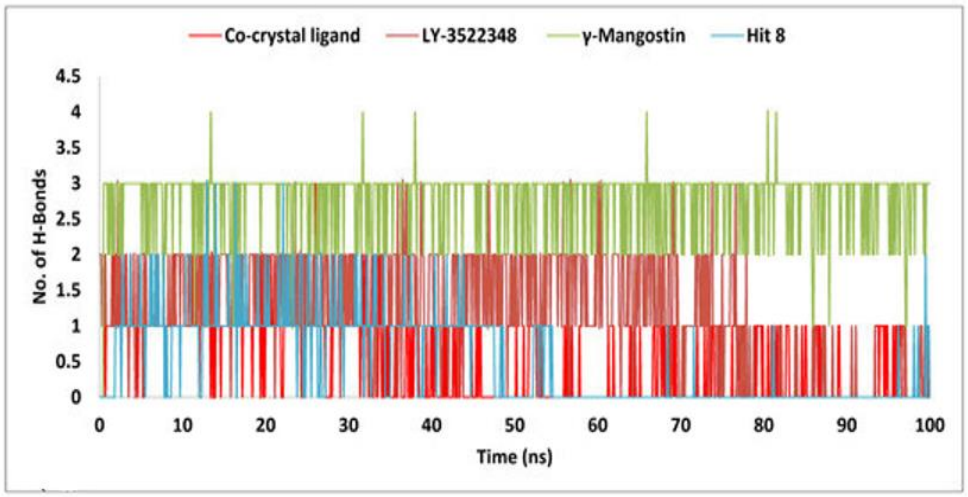

a)

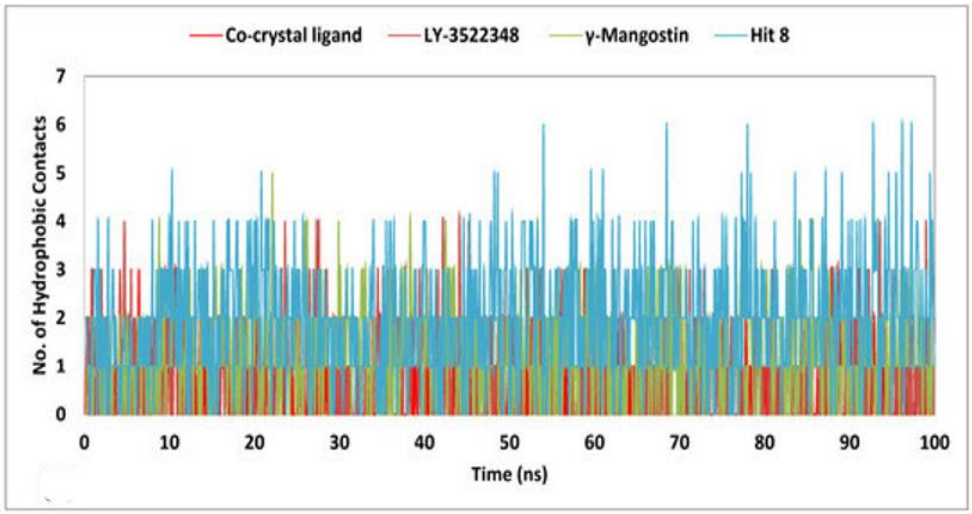

b)

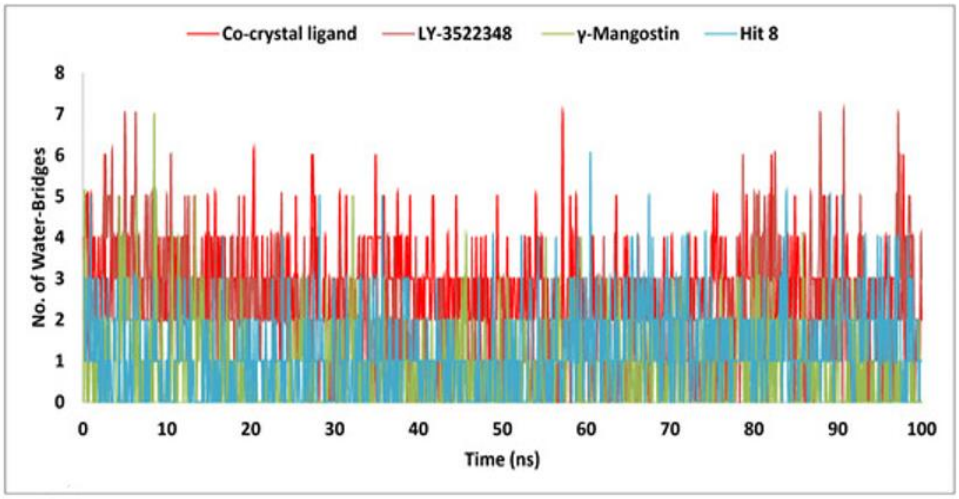

c)

Figure 13. Evaluation of hydrogen bonds (a), hydrophobic interactions (b), and water-mediated bridges (c) for the co-crystallized ligand, LY-3522348, γ-Mangostin, and hit 8 across 100 ns molecular dynamics simulations.

Quantum mechanical calculations

Quantum mechanical methods are commonly employed to examine the molecular orbital distributions and electronic characteristics of candidate compounds [77, 78]. In this work, hit 8 stood out as the leading molecule

among the screened hits, exhibiting superior binding affinity, improved pharmacokinetic profile, desirable physicochemical attributes, high absorption potential, and robust metabolic stability. Its consistent performance within the KHK-C active site during dynamics simulations further reinforced its promise. Consequently, hit 8 was selected for quantum mechanical computations to probe its electronic parameters, interaction energies, and chemical reactivity, providing a more comprehensive understanding of its binding mode and opportunities for refining its drug-like properties.

A compound's electron affinity correlates with its LUMO energy level, whereas its ionization potential relates to the HOMO [79]. For hit 8, the HOMO energy was calculated at −6.02 eV and the LUMO at −1.62 eV, yielding a HOMO–LUMO energy gap (HLG) of 4.4 eV **(Table 4).** This moderate gap suggests reasonable electronic stability combined with adequate reactivity, enabling effective participation in electron-transfer events [80]. The solvation energy of −17.80 kcal/mol indicates substantial solvent–molecule interactions, pointing to considerable stabilization in aqueous or polar environments—a valuable trait for biological and catalytic contexts.

Additional quantum descriptors were derived using established equations from the literature [81]. The chemical hardness (η) of 2.2 eV and softness (σ) of 0.45 eV^{-1} **(Table 4)** reflect a comparatively resistant electronic framework, while the global electrophilicity index (ω) of 3.32 eV confirms strong electron-accepting capability during reactions.

The spatial distribution of molecular orbitals **(Figure 14)** offers deeper insights into the electronic profile of hit 8. The HOMO is mainly distributed over the hydroxyl (OH) moieties, the oxygen in the methoxy substituent, the oxygen within the xanthene ring, the carbonyl functionality of the xanthone core, and the aromatic portions of the xanthene scaffold. These areas serve as primary electron-donating sites, supporting reactivity and resistance to oxidation. Conversely, the LUMO is concentrated on the oxygen atom of the pyrano ring, the xanthone carbonyl, the xanthene ring oxygen, and the two hydroxyl groups, functioning as electron-accepting regions that govern interactions with nucleophiles and reduction behavior.

The electronic characteristics of hit 8 are profoundly shaped by its molecular architecture. The conjugated π-system in the xanthene framework significantly influences the HOMO–LUMO gap, promoting broad electron delocalization and conferring moderate stability. Electron-donating substituents, including the 8-methoxy and 5,9-dihydroxy groups, elevate the HOMO energy level, bolstering resistance to oxidation while retaining reactivity. The prenyl chain and dimethyl moieties provide steric protection, shielding vulnerable sites and enhancing overall structural integrity. Together, these elements account for the compound's pronounced electrophilicity, balanced hardness, and controlled reactivity.

The notable solvation energy of −17.80 kcal/mol aligns closely with the structural and electronic makeup of hit 8. The extended conjugated xanthene system and polar functional groups increase molecular polarizability, facilitating robust solvent engagement and a stable solvation layer. The hydroxyl and methoxy groups function as both hydrogen bond donors and acceptors, strengthening dipolar and hydrogen-bonding contacts with surrounding solvent molecules. The hydrophobic prenyl substituent moderates overall solubility, achieving an optimal balance. This interplay between electronic distribution and structural motifs underpins the compound's favorable solution-phase stability, underscoring its suitability for diverse chemical and biological applications.

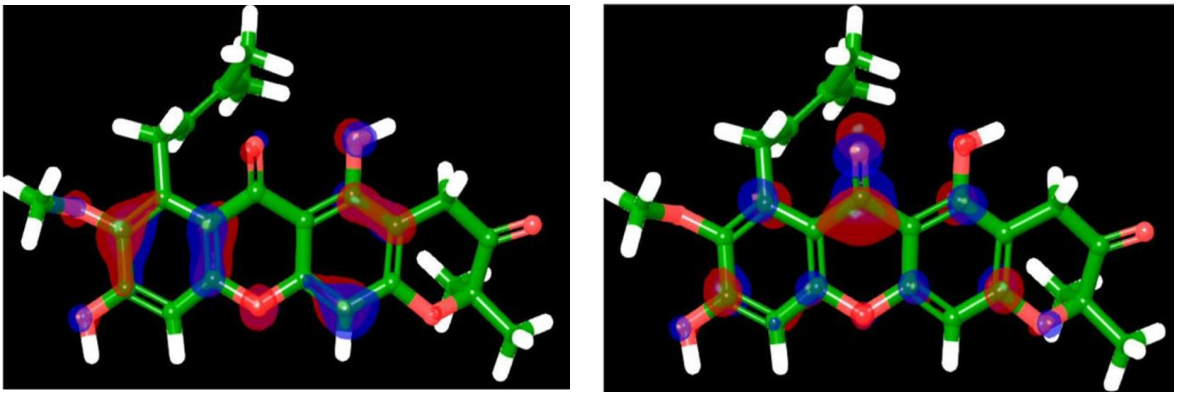

a) b)

Figure 14. Spatial Distribution of HOMO (A) and LUMO (B) orbitals in hit 8.

Table 4. Quantum mechanical descriptors of hit 8: electronic and solvation properties.

Property	Solvation Energy kcal/mol	HOMO (eV)	LUMO (eV)	HLG	Electron Affinity (eV)	Ionization Potential (eV)	Chemical Hardness (eV)	Chemical Softness (eV^{-1})	Electronegativity (eV)	Global Electrophilicity Index (eV)
Hit 8	−17.80	−6.02	−1.62	4.4	1.62	6.02	2.2	0.45	−3.82	3.32

Conclusion

Through this investigation, multiple new derivatives were discovered exhibiting strong inhibitory activity toward the KHK-C protein, outperforming α-Mangostin in terms of binding strength. Notably, hit 8 displayed the most favorable binding free energy, alongside advantageous pharmacokinetic traits like complete predicted human oral bioavailability and improved resistance to metabolism. Results from molecular dynamics confirmed the robust occupancy of hit 8 within the KHK-C pocket, supporting its viability as a potential therapeutic agent. Additional quantum calculations underscored its wider utility. Overall, these outcomes lay a solid groundwork for subsequent laboratory testing and advancement of KHK-C targeted therapies against metabolic conditions linked to excessive fructose intake.

Acknowledgments: None

Conflict of Interest: None

Financial Support: None

Ethics Statement: None

References

1. Giussani, M.; Lieti, G.; Orlando, A.; Parati, G.; Genovesi, S. Fructose Intake, Hypertension and Cardiometabolic Risk Factors in Children and Adolescents: From Pathophysiology to Clinical Aspects. A Narrative Review. Front. Med. **2022**, 9, 792949.
2. Basciano, H.; Federico, L.; Adeli, K. Fructose, insulin resistance, and metabolic dyslipidemia. Nutr. Metab. **2005**, 2, 5.
3. Khan, T.A.; Sievenpiper, J.L. Controversies about sugars: Results from systematic reviews and meta-analyses on obesity, cardiometabolic disease and diabetes. Eur. J. Nutr. **2016**, 55, 25–43.
4. Bernstein, A.M.; de Koning, L.; Flint, A.J.; Rexrode, K.M.; Willett, W.C. Soda consumption and the risk of stroke in men and women. Am. J. Clin. Nutr. **2012**, 95, 1190–1199.
5. Alturki, M.S. Exploring Marine-Derived Compounds: In Silico Discovery of Selective Ketohexokinase (KHK) Inhibitors for Metabolic Disease Therapy. Mar. Drugs **2024**, 22, 455.
6. Gutierrez, J.A.; Liu, W.; Perez, S.; Xing, G.; Sonnenberg, G.; Kou, K.; Blatnik, M.; Allen, R.; Weng, Y.; Vera, N.B.; et al. Pharmacologic inhibition of ketohexokinase prevents fructose-induced metabolic dysfunction. Mol. Metab. **2021**, 48, 101196.
7. Mohan, A. WHO recommends reducing intake of'free sugars' by adults and children. Natl. Med. J. India **2015**, 28, 165.
8. Vos, M.B. Nutrition, nonalcoholic fatty liver disease and the microbiome: Recent progress in the field. Curr. Opin. Lipidol. **2014**, 25, 61–66.
9. Stanhope, K.L.; Schwarz, J.M.; Keim, N.L.; Griffen, S.C.; Bremer, A.A.; Graham, J.L.; Hatcher, B.; Cox, C.L.; Dyachenko, A.; Zhang, W. Consuming fructose-sweetened, not glucose-sweetened, beverages increases visceral adiposity and lipids and decreases insulin sensitivity in overweight/obese humans. J. Clin. Investig. **2009**, 119, 1322–1334.

10. Taskinen, M.R.; Söderlund, S.; Bogl, L.; Hakkarainen, A.; Matikainen, N.; Pietiläinen, K.; Räsänen, S.; Lundbom, N.; Björnson, E.; Eliasson, B. Adverse effects of fructose on cardiometabolic risk factors and hepatic lipid metabolism in subjects with abdominal obesity. J. Intern. Med. **2017**, 282, 187–201.
11. Swarbrick, M.M.; Stanhope, K.L.; Elliott, S.S.; Graham, J.L.; Krauss, R.M.; Christiansen, M.P.; Griffen, S.C.; Keim, N.L.; Havel, P.J. Consumption of fructose-sweetened beverages for 10 weeks increases postprandial triacylglycerol and apolipoprotein-B concentrations in overweight and obese women. Br. J. Nutr. **2008**, 100, 947–952.
12. Lustig, R.H.; Mulligan, K.; Noworolski, S.M.; Tai, V.W.; Wen, M.J.; Erkin-Cakmak, A.; Gugliucci, A.; Schwarz, J.M. Isocaloric fructose restriction and metabolic improvement in children with obesity and metabolic syndrome. Obesity **2016**, 24, 453–460.
13. Schwarz, J.-M.; Noworolski, S.M.; Erkin-Cakmak, A.; Korn, N.J.; Wen, M.J.; Tai, V.W.; Jones, G.M.; Palii, S.P.; Velasco-Alin, M.; Pan, K. Effects of dietary fructose restriction on liver fat, de novo lipogenesis, and insulin kinetics in children with obesity. Gastroenterology **2017**, 153, 743–752.
14. Gugliucci, A.; Lustig, R.H.; Caccavello, R.; Erkin-Cakmak, A.; Noworolski, S.M.; Tai, V.W.; Wen, M.J.; Mulligan, K.; Schwarz, J.-M. Short-term isocaloric fructose restriction lowers apoC-III levels and yields less atherogenic lipoprotein profiles in children with obesity and metabolic syndrome. Atherosclerosis **2016**, 253, 171–177.
15. Ishimoto, T.; Lanaspa, M.A.; Le, M.T.; Garcia, G.E.; Diggle, C.P.; MacLean, P.S.; Jackman, M.R.; Asipu, A.; Roncal-Jimenez, C.A.; Kosugi, T. Opposing effects of fructokinase C and A isoforms on fructose-induced metabolic syndrome in mice. Proc. Natl. Acad. Sci. USA **2012**, 109, 4320–4325.
16. Ferreira, J.C.; Villanueva, A.J.; Fadl, S.; Al Adem, K.; Cinviz, Z.N.; Nedyalkova, L.; Cardoso, T.H.; Andrade, M.E.; Saksena, N.K.; Sensoy, O. Residues in the fructose-binding pocket are required for ketohexokinase-A activity. J. Biol. Chem. **2024**, 300, 107538.
17. Romero, F.A.; Jones, C.T.; Xu, Y.; Fenaux, M.; Halcomb, R.L. The Race to Bash NASH: Emerging Targets and Drug Development in a Complex Liver Disease. J. Med. Chem. **2020**, 63, 5031–5073.
18. Diggle, C.P.; Shires, M.; Leitch, D.; Brooke, D.; Carr, I.M.; Markham, A.F.; Hayward, B.E.; Asipu, A.; Bonthron, D.T. Ketohexokinase: Expression and localization of the principal fructose-metabolizing enzyme. J. Histochem. Cytochem. **2009**, 57, 763–774.
19. Ishimoto, T.; Lanaspa, M.A.; Rivard, C.J.; Roncal-Jimenez, C.A.; Orlicky, D.J.; Cicerchi, C.; McMahan, R.H.; Abdelmalek, M.F.; Rosen, H.R.; Jackman, M.R. High-fat and high-sucrose (western) diet induces steatohepatitis that is dependent on fructokinase. Hepatology **2013**, 58, 1632–1643.
20. Huard, K.; Ahn, K.; Amor, P.; Beebe, D.A.; Borzilleri, K.A.; Chrunyk, B.A.; Coffey, S.B.; Cong, Y.; Conn, E.L.; Culp, J.S.; et al. Discovery of Fragment-Derived Small Molecules for in Vivo Inhibition of Ketohexokinase (KHK). J. Med. Chem. **2017**, 60, 7835–7849.
21. Zhu, G.; Li, J.; Lin, X.; Zhang, Z.; Hu, T.; Huo, S.; Li, Y. Discovery of a Novel Ketohexokinase Inhibitor with Improved Drug Distribution in Target Tissue for the Treatment of Fructose Metabolic Disease. J. Med. Chem. **2023**, 66, 13501–13515.
22. Durham, T. 2, 6-Diamino Pyridine Compounds. Patent WO2020051058 A, 22 September 2020.
23. Durham, T.B.; Hao, J.; Spinazze, P.; Stack, D.R.; Toth, J.L.; Massey, S.; Mbofana, C.T.; Johnston, R.D.; Lineswala, J.P.; Wrobleski, A.; et al. Identification of LY3522348: A Highly Selective and Orally Efficacious Ketohexokinase Inhibitor. J. Med. Chem. **2023**, 66, 15960–15976.
24. Heine, N.; Weber, A.; Pautsch, A.; Gottschling, D.; Uphues, I.; Bauer, M.; Ebenhoch, R.; Magarkar, A.; Nosse, B.; Kley, J.T. Discovery of BI-9787, a potent zwitterionic ketohexokinase inhibitor with oral bioavailability. Bioorg Med. Chem. Lett. **2024**, 112, 129930.
25. Le, M.T.; Lanaspa, M.A.; Cicerchi, C.M.; Rana, J.; Scholten, J.D.; Hunter, B.L.; Rivard, C.J.; Randolph, R.K.; Johnson, R.J. Bioactivity-Guided Identification of Botanical Inhibitors of Ketohexokinase. PLoS ONE **2016**, 11, e0157458.
26. Maryanoff, B.E.; O'Neill, J.C.; McComsey, D.F.; Yabut, S.C.; Luci, D.K.; Jordan, A.D., Jr.; Masucci, J.A.; Jones, W.J.; Abad, M.C.; Gibbs, A.C.; et al. Inhibitors of Ketohexokinase: Discovery of Pyrimidinopyrimidines with Specific Substitution that Complements the ATP-Binding Site. ACS Med. Chem. Lett. **2011**, 2, 538–543.
27. Dzobo, K. The Role of Natural Products as Sources of Therapeutic Agents for Innovative Drug Discovery. In Comprehensive Pharmacology; Elsevier: Amsterdam, The Netherlands, 2022; pp. 408–422.

28. Atanasov, A.G.; Zotchev, S.B.; Dirsch, V.M.; International Natural Product Sciences, T.; Supuran, C.T. Natural products in drug discovery: Advances and opportunities. Nat. Rev. Drug Discov. **2021**, 20, 200–216.
29. Tang, S.Y.; Whiteman, M.; Jenner, A.; Peng, Z.F.; Halliwell, B. Mechanism of cell death induced by an antioxidant extract of Cratoxylum cochinchinense (YCT) in Jurkat T cells: The role of reactive oxygen species and calcium. Free Radic. Biol. Med. **2004**, 36, 1588–1611.
30. Martínez Sánchez, G.; Rodríguez, H.M.A.; Giuliani, A.; Núñez Sellés, A.J.; Pons Rodríguez, N.; Fernández, O.S.L.; Re, L. Protective effect of Mangifera indica L. extract (Vimang®) on the injury associated with hepatic ischaemia reperfusion. Phytother. Res. **2003**, 17, 197–201.
31. Madan, B.; Singh, I.; Kumar, A.; Prasad, A.K.; Raj, H.G.; Parmar, V.S.; Ghosh, B. Xanthones as inhibitors of microsomal lipid peroxidation and TNF-α induced ICAM-1 expression on human umbilical vein endothelial cells (HUVECs). Bioorg Med. Chem. **2002**, 10, 3431–3436.
32. Chin, Y.-W.; Jung, H.-A.; Chai, H.; Keller, W.J.; Kinghorn, A.D. Xanthones with quinone reductase-inducing activity from the fruits of Garcinia mangostana (Mangosteen). Phytochemistry **2008**, 69, 754–758.
33. Ignatushchenko, M.V.; Winter, R.W.; Riscoe, M. Xanthones as antimalarial agents: Stage specificity. Am. J. Trop. Med. Hyg. **2000**, 62, 77–81.
34. Sakagami, Y.; Iinuma, M.; Piyasena, K.; Dharmaratne, H. Antibacterial activity of α-mangostin against vancomycin resistant Enterococci (VRE) and synergism with antibiotics. Phytomedicine **2005**, 12, 203–208.
35. Elsaman, T.; Mohamed, M.S.; Eltayib, E.M.; Abdalla, A.E.; Mohamed, M.A. Xanthone: A Promising Antimycobacterial Scaffold. Med. Chem. **2021**, 17, 310–331.
36. Sudta, P.; Jiarawapi, P.; Suksamrarn, A.; Hongmanee, P.; Suksamrarn, S. Potent activity against multidrug-resistant Mycobacterium tuberculosis of α-mangostin analogs. Chem. Pharm. Bull. **2013**, 61, 194–203.
37. Roney, M.; Mohd Aluwi, M.F.F. The importance of in-silico studies in drug discovery. Intell. Pharm. **2024**, 2, 578–579.
38. Sorokina, M.; Merseburger, P.; Rajan, K.; Yirik, M.A.; Steinbeck, C. COCONUT online: Collection of Open Natural Products database. J. Cheminform. **2021**, 13, 2.
39. Kim, S.; Chen, J.; Cheng, T.; Gindulyte, A.; He, J.; He, S.; Li, Q.; Shoemaker, B.A.; Thiessen, P.A.; Yu, B. PubChem 2023 update. Nucleic Acids Res. **2023**, 51, D1373–D1380.
40. Tran, V.A.; Thi Vo, T.-T.; Nguyen, M.-N.T.; Duy Dat, N.; Doan, V.-D.; Nguyen, T.-Q.; Vu, Q.H.; Le, V.T.; Tong, T.D.; Maneiro, M. Novel α-Mangostin Derivatives from Mangosteen (Garcinia mangostana L.) Peel Extract with Antioxidant and Anticancer Potential. J. Med. Chem. **2021**, 2021, 9985604.
41. Chi, X.Q.; Hou, B.; Yang, L.; Zi, C.T.; Lv, Y.F.; Li, J.Y.; Ren, F.C.; Yuan, M.Y.; Hu, J.M.; Zhou, J. Design, synthesis and cholinesterase inhibitory activity of alpha-mangostin derivatives. Nat. Prod. Res. **2020**, 34, 1380–8.
42. Tocmo, R.; Le, B.; Heun, A.; van Pijkeren, J.P.; Parkin, K.; Johnson, J.J. Prenylated xanthones from mangosteen (Garcinia mangostana) activate the AhR and Nrf2 pathways and protect intestinal barrier integrity in HT-29 cells. Free Radic. Biol. Med. **2021**, 163, 102–15.
43. Le, T.T.; Pandey, R.P.; Gurung, R.B.; Dhakal, D.; Sohng, J.K. Efficient enzymatic systems for synthesis of novel alpha-mangostin glycosides exhibiting antibacterial activity against Gram-positive bacteria. Appl. Microbiol. Biotechnol. **2014**, 98, 8527–38.
44. Madhavi Sastry, G.; Adzhigirey, M.; Day, T.; Annabhimoju, R.; Sherman, W. Protein and ligand preparation: Parameters, protocols, and influence on virtual screening enrichments. J. Comput. Aided Mol. Des. **2013**, 27, 221–34.
45. LigPrep; 2023-1; Schrödinger, LLC: New York, NY, USA, 2023.
46. Friesner, R.A.; Banks, J.L.; Murphy, R.B.; Halgren, T.A.; Klicic, J.J.; Mainz, D.T.; Repasky, M.P.; Knoll, E.H.; Shelley, M.; Perry, J.K. Glide: A new approach for rapid, accurate docking and scoring. 1. Method and assessment of docking accuracy. J. Med. Chem. **2004**, 47, 1739–49.
47. Halgren, T.A.; Murphy, R.B.; Friesner, R.A.; Beard, H.S.; Frye, L.L.; Pollard, W.T.; Banks, J.L. Glide: A new approach for rapid, accurate docking and scoring. 2. Enrichment factors in database screening. J. Med. Chem. **2004**, 47, 1750–9.
48. Jacobson, M.P.; Pincus, D.L.; Rapp, C.S.; Day, T.J.; Honig, B.; Shaw, D.E.; Friesner, R.A. A hierarchical approach to all-atom protein loop prediction. Proteins Struct. Funct. Bioinf. **2004**, 55, 351–67.
49. Jacobson, M.P.; Friesner, R.A.; Xiang, Z.; Honig, B. On the role of the crystal environment in determining protein side-chain conformations. J. Mol. Biol. **2002**, 320, 597–608.

50. Ioakimidis, L.; Thoukydidis, L.; Mirza, A.; Naeem, S.; Reynisson, J. Benchmarking the reliability of QikProp. Correlation between experimental and predicted values. QSAR Comb. Sci. **2008**, 27, 445–56.
51. Bochevarov, A.D.; Harder, E.; Hughes, T.F.; Greenwood, J.R.; Braden, D.A.; Philipp, D.M.; Rinaldo, D.; Halls, M.D.; Zhang, J.; Friesner, R.A. Jaguar: A high-performance quantum chemistry software program with strengths in life and materials sciences. Int. J. Quantum Chem. **2013**, 113, 2110–42.
52. Bowers, K.J.; Chow, E.; Xu, H.; Dror, R.O.; Eastwood, M.P.; Gregersen, B.A.; Klepeis, J.L.; Kolossvary, I.; Moraes, M.A.; Sacerdoti, F.D. Scalable algorithms for molecular dynamics simulations on commodity clusters. In Proceedings of the 2006 ACM/IEEE Conference on Supercomputing, Tampa, FL, USA, 11–17 November 2006; p. 84-es.
53. Maestro; 2023-1; Schrödinger, LLC: New York, NY, USA, 2023.
54. Elsaman, T.; Ahmad, I.; Eltayib, E.M.; Suliman Mohamed, M.; Yusuf, O.; Saeed, M.; Patel, H.; Mohamed, M.A. Flavonostilbenes natural hybrids from Rhamnoneuron balansae as potential antitumors targeting ALDH1A1: Molecular docking, ADMET, MM-GBSA calculations and molecular dynamics studies. J. Biomol. Struct. Dyn. **2024**, 42, 3249–66.
55. Schmidt, J.; VandeVondele, J.; Kuo, I.-F.W.; Sebastiani, D.; Siepmann, J.I.; Hutter, J.; Mundy, C.J. Isobaric–isothermal molecular dynamics simulations utilizing density functional theory: An assessment of the structure and density of water at near-ambient conditions. J. Phys. Chem. B **2009**, 113, 11959–64.
56. Bouback, T.A.; Pokhrel, S.; Albeshri, A.; Aljohani, A.M.; Samad, A.; Alam, R.; Hossen, M.S.; Al-Ghamdi, K.; Talukder, M.E.K.; Ahammad, F.; et al. Pharmacophore-Based Virtual Screening, Quantum Mechanics Calculations, and Molecular Dynamics Simulation Approaches Identified Potential Natural Antiviral Drug Candidates against MERS-CoV S1-NTD. Molecules **2021**, 26, 4961.
57. Andres-Hernando, A.; Orlicky, D.J.; Kuwabara, M.; Ishimoto, T.; Nakagawa, T.; Johnson, R.J.; Lanaspa, M.A. Deletion of fructokinase in the liver or in the intestine reveals differential effects on sugar-induced metabolic dysfunction. Cell Metab. **2020**, 32, 117–27.e113.
58. Brymora, A.; Flisiński, M.; Johnson, R.J.; Goszka, G.; Stefańska, A.; Manitius, J. Low-fructose diet lowers blood pressure and inflammation in patients with chronic kidney disease. Nephrol. Dial. Transplant. **2012**, 27, 608–12.
59. Shepherd, E.L.; Saborano, R.; Northall, E.; Matsuda, K.; Ogino, H.; Yashiro, H.; Pickens, J.; Feaver, R.E.; Cole, B.K.; Hoang, S.A. Ketohexokinase inhibition improves NASH by reducing fructose-induced steatosis and fibrogenesis. JHEP Rep. **2021**, 3, 100217.
60. Johnson, R.J.; Bakris, G.L.; Borghi, C.; Chonchol, M.B.; Feldman, D.; Lanaspa, M.A.; et al. Hyperuricemia, acute and chronic kidney disease, hypertension, and cardiovascular disease: Report of a scientific workshop organized by the National Kidney Foundation. Am. J. Kidney Dis. **2018**, 71, 851–65.
61. Sahu, D.; Rathor, L.S.; Dwivedi, S.D.; Shah, K.; Chauhan, N.S.; Singh, M.R.; Singh, D. A review on molecular docking as an interpretative tool for molecular targets in disease management. Assay. Drug Dev. Technol. **2024**, 22, 40–50.
62. Stanzione, F.; Giangreco, I.; Cole, J.C. Use of molecular docking computational tools in drug discovery. Prog. Med. Chem. **2021**, 60, 273–343.
63. Mohamed, M.A.; Elsaman, T.; Mohamed, M.S.; Eltayib, E.M. Computational investigations of flavonoids as ALDH isoform inhibitors for treatment of cancer. SAR QSAR Environ. Res. **2024**, 35, 837–75.
64. Badiali, C.; Petruccelli, V.; Brasili, E.; Pasqua, G. Xanthones: Biosynthesis and Trafficking in Plants, Fungi and Lichens. Plants **2023**, 12, 694.
65. Wu, F.; Zhou, Y.; Li, L.; Shen, X.; Chen, G.; Wang, X.; Liang, X.; Tan, M.; Huang, Z. Computational Approaches in Preclinical Studies on Drug Discovery and Development. Front. Chem. **2020**, 8, 726.
66. Madden, J.C. In silico approaches for predicting ADME properties. In Recent Advances in QSAR Studies: Methods and Applications; Springer: Berlin/Heidelberg, Germany, 2010; pp. 283–304.
67. Jung, W.; Goo, S.; Hwang, T.; Lee, H.; Kim, Y.K.; Chae, J.W.; Yun, H.Y.; Jung, S. Absorption Distribution Metabolism Excretion and Toxicity Property Prediction Utilizing a Pre-Trained Natural Language Processing Model and Its Applications in Early-Stage Drug Development. Pharmaceuticals **2024**, 17, 382.
68. Ntie-Kang, F.; Lifongo, L.L.; Mbah, J.A.; Owono Owono, L.C.; Megnassan, E.; Mbaze, L.M.a.; Judson, P.N.; Sippl, W.; Efange, S.M. In silico drug metabolism and pharmacokinetic profiles of natural products from medicinal plants in the Congo basin. Silico Pharmacol. **2013**, 1, 12.

69. Ntie-Kang, F. An in silico evaluation of the ADMET profile of the StreptomeDB database. Springerplus **2013**, 2, 353.
70. Butnarasu, C.; Garbero, O.V.; Petrini, P.; Visai, L.; Visentin, S. Permeability Assessment of a High-Throughput Mucosal Platform. Pharmaceutics **2023**, 15, 380.
71. Ertl, P.; Rohde, B.; Selzer, P. Fast calculation of molecular polar surface area as a sum of fragment-based contributions and its application to the prediction of drug transport properties. J. Med. Chem. **2000**, 43, 3714–7.
72. Prasanna, S.; Doerksen, R.J. Topological polar surface area: A useful descriptor in 2D-QSAR. Curr. Med. Chem. **2009**, 16, 21–41.
73. Asano, D.; Takakusa, H.; Nakai, D. Oral Absorption of Middle-to-Large Molecules and Its Improvement, with a Focus on New Modality Drugs. Pharmaceutics **2023**, 16, 47.
74. Wanat, K.; Zydek, G.; Hekner, A.; Brzezinska, E. In silico Plasma Protein Binding Studies of Selected Group of Drugs Using TLC and HPLC Retention Data. Pharmaceuticals **2021**, 14, 202.
75. Wang, T.; Sun, J.; Zhao, Q. Investigating cardiotoxicity related with hERG channel blockers using molecular fingerprints and graph attention mechanism. Comput. Biol. Med. **2023**, 153, 106464.
76. Masimirembwa, C.M.; Bredberg, U.; Andersson, T.B. Metabolic stability for drug discovery and development: Pharmacokinetic and biochemical challenges. Clin. Pharmacokinet. **2003**, 42, 515–28.
77. Merz, K.M., Jr. Using quantum mechanical approaches to study biological systems. Acc. Chem. Res. **2014**, 47, 2804–11.
78. Ginex, T.; Vazquez, J.; Estarellas, C.; Luque, F.J. Quantum mechanical-based strategies in drug discovery: Finding the pace to new challenges in drug design. Curr. Opin. Struct. Biol. **2024**, 87, 102870.
79. Zhan, C.-G.; Nichols, J.A.; Dixon, D.A. Ionization potential, electron affinity, electronegativity, hardness, and electron excitation energy: Molecular properties from density functional theory orbital energies. J. Phys. Chem. A **2003**, 107, 4184–95.
80. Lefi, N.; Kazachenko, A.S.; Raja, M.; Issaoui, N.; Kazachenko, A.S. Molecular Structure, Spectral Analysis, Molecular Docking and Physicochemical Studies of 3-Bromo-2-hydroxypyridine Monomer and Dimer as Bromodomain Inhibitors. Molecules **2023**, 28, 2669.
81. Kumer, A.; Chakma, U.; Rana, M.M.; Chandro, A.; Akash, S.; Elseehy, M.M.; Albogami, S.; El-Shehawi, A.M. Investigation of the New Inhibitors by Sulfadiazine and Modified Derivatives of alpha-D-glucopyranoside for White Spot Syndrome Virus Disease of Shrimp by In Silico: Quantum Calculations, Molecular Docking, ADMET and Molecular Dynamics Study. Molecules **2022**, 27, 3694.